EUROPEAN ORGANIZATION FOR NUCLEAR RESEARCH

CERN–PPE/94–226
24 November 1994

QUARTZ FIBER CALORIMETRY

P. Gorodetzky[a,b], D. Lazic[a,c], G. Anzivino[d], E. Chiavassa[e], A. Contin[f,g], G. Dellacasa[e,h], N. Demarco[e], R. De Salvo[g], M. Gallio[e], P. Guaita[e], K.F. Johnson[c], P. Juillot[a], M. Lundin[a,i], M. Marino[j,k], A. Musso[e], A. Piccotti[e], E. Scomparin[e], E. Vercellin[e]

[a] CRN and Université Louis Pasteur, Strasbourg, France.
[b] CERN, Geneva, Switzerland.
[c] Florida State University, Tallahassee, FL, USA.
[d] INFN Laboratori Nazionali di Frascati, Italy.
[e] Università di Torino and INFN Torino, Italy.
[f] Università di Bologna and INFN, Sezione di Bologna, Italy.
[g] CERN/LAA, Geneva, Switzerland.
[h] Presently at Università di Alessandria, Italy.
[i] Partially supported by World Laboratory Fellowships, Lausanne, Switzerland.
[j] World Laboratory, Lausanne, Switzerland.
[k] Now at CERN, Geneva, Switzerland.

Abstract

The fundamentals of a new electromagnetic and hadronic sampling calorimetry based on the detection of Cherenkov light generated in quartz optical fibers are presented. Optical fibers transport light only in a selected angular range which results in a non-obvious and absolutely unique characteristic for this new technique: showers of very narrow visible energy. In addition, the technique is characterized by radiation resistance measured in Gigarads and nanosecond signal duration. Combined, these properties make quartz fiber calorimetry a very promising technique for high intensity heavy ion experiments and for the high pseudorapidity regions of high intensity collider experiments. The results of beam tests and simulations are used to illustrate the basic properties and peculiar characteristics of this recent development.

(Submitted to Nuclear Instruments and Methods)

1 INTRODUCTION.

The processes studied today and in the near future in high energy physics are often characterized by very low cross sections, where the events containing new physics can be as rare as once in 10^8 to 10^{10} collisions, masked by uninteresting processes with very high cross sections. As a direct result, interesting physics signals can be produced only by the use of very intense beams and high collision rates. Therefore, the detectors used in such situations must satisfy demanding requirements in order to fulfill their physics objectives. The difficulties become particularly severe in the high pseudorapidity regions of future hadron collider detectors, as well as in existing and future high intensity heavy-ion experiments.

The intensity of the beams, the rate of collisions and the total deposited energies are such that the detectors in these regions must be extremely radiation resistant and fast. This becomes even more important when considering calorimetry, where some of the basic phenomena accompanying hadron shower development (such as neutron propagation) may considerably compromise detector speed. There are two basic applications of calorimeters in high pseudorapidity regions: those used for fixed-target and those for collider experiments.

The calorimeters at very high pseudorapidity for heavy-ion physics, Zero Degree Calorimeters (ZDCs), are used for measurements of the energies of spectator fragments of the projectile ions in order to have fast and direct information on the energy and centrality of the collision. They are situated behind the target and cover a very small solid angle, thereby receiving the non-interacting projectiles. The size of a ZDC should be reduced as much as possible to avoid reaction products but should be large enough to contain the non-interacting particles' showers. Therefore a reduced visible shower size would be a substantial benefit. Experiments searching for quark gluon plasma work with very high intensities and total energies, dictating that a ZDC should be able to accept and correctly measure up to 10^7 to 10^8 ions per second, each carrying as much as 33 TeV [1]. All of the projectiles impact the detector at approximately the same spot and so position resolution is not an issue, however the very demanding requirements on both speed and radiation resistance of these detectors are obvious.

Somewhat less stringent requirements, with respect to radiation resistance and speed, are encountered in very-forward regions ($\mid \eta \mid > 2.5$) for Large Hadron Collider (LHC) experiments. The doses will be an order of magnitude lower (1-2 MGy/5 years [2]) and the time between bunch crossings will be 25 ns. However, the detectors are expected to accomplish more sophisticated goals than the measurement of the overall energy of the incoming particles. Their principal task is to extend the detector pseudorapidity coverage, improving the precision of missing transverse energy measurements, and to provide forward jet tagging for event selection. This means that Very Forward Calorimeters (VFCals) for LHC have to be able to give precise shower position information in the $\eta - \phi$ space.

In this article we present and discuss the principle and results of studies of a new calorimetry technique that easily satisfies all the requirements for performance in the high pseudorapidity region: Quartz fiber Calorimetry (QCal). The denomination "quartz" is not completely correct though, for it refers to a crystal. Technically, the correct term is "amorphous silica," usually referred to as silica. In this article we use the term quartz to refer to amorphous silica.

The basic principle for quartz fiber calorimetry is rather simple: the charged particles from a shower generated in a dense, high Z absorber produce Cherenkov light in quartz optical fibers interspersed in the absorber. The same fibers act as optical guides for the generated light which propagates towards photon-detectors. The basic motivations for the choice of this technique are two-fold: the radiation resistance of quartz and the intrinsic speed of the Cherenkov effect. Relatively small light yields, resulting in greater energy resolution stochastic terms, are not a deficiency of this technique as these detectors are intended to work in a very high energy range. This article reports results produced by the QCal collaboration and CERN RD40, which aggregated to explore the capabilities of the quartz fiber calorimetry technique [3, 4, 5, 6, 7, 8, 9, 10, 11, 12, 13, 14, 15] after its initial conception in 1990.

In Section 2 we discuss the radiation resistance of quartz and quartz fibers. Section 3 gives a brief overview of the peculiarities of the Cherenkov effect in optical fibers. Section 4 discusses the quartz fiber calorimetry technique's inherent, nanosecond response capabilities. In Section 5 we discuss applications of this technique in calorimetry and give results of beam tests on different electromagnetic and hadronic prototypes. In Section 6 we draw conclusions on results obtained so far and the directions for further work.

2 RADIATION HARDNESS OF QUARTZ.

Wavelength dependent transmittance of high quality quartz discs was measured in 1986 with a 100 MeV/nucleon O^{16} beam at GANIL. The measurements showed transmittance of quartz in the visible region to be maintained up to 20 Grads [3, 5]. The dose rate in this test was 600 Mrads/hour, a very high short term dose. Based on the experience of NA38 (quark-gluon plasma search through measurement of J/ψ suppression) at CERN, we believe that the transmittance of this type of quartz would not be worse for the same dose delivered over a period of years. NA38 uses quartz counters read out by quartz fibers to identify and center a sulfur ion beam. The gain of the PMTs used for the readout of Cherenkov radiation in quartz has not been changed as a compensation for increases or decreases in light output after an integrated radiation dose of more than 50 Grad over 8 years.

An irradiation was conducted to examine the relative damage to various commercially available quartz fibers as a function of dose. Five different types of fibers were selected and four fibers of each type were irradiated; one with fluorine doped, quartz cladding and four different types of plastic clad fibers. All the fibers were produced by Ensign Bickford (now Spectran), USA. The irradiations were performed using the 2 MeV electron beam of the Vivirad irradiation facility in Strasbourg, France.

The light output measured in the test was produced by the Cherenkov light of the irradiating electrons crossing the one meter long fibers at 45° and at a fixed, single location on the fibers. In this way, radiation damage affecting the Cherenkov light production and loss in transmittance for this light was observed simultaneously. The downstream ends of each of the fibers were directed away from the irradiation source. The result was a set of light spots which were recorded (via a mirror) by a commercially available Charge Coupled Device (CCD) camera with visible light optics and with manual control settings which were set and fixed for all camera parameters. A reference light source was installed to monitor camera stability, reflectivity of the mirror and transparency of the screen. It consisted of a

quartz fiber illuminated by a Light Emitting Diode (LED). The fiber, the mirror and the LED were all shielded from the irradiation source. A peak dose (the RMS width of the beam was 3 cm) of 2.2 Gigarads was delivered over a period of 130 minutes to a point on the fibers which was 60 cm from the readout end.

Figure 1 shows the relative Cherenkov light yield for the five different types of fibers as a function of dose. HCG is an ultra-pure (impurities below the ppm level) quartz fiber with a fluorinated quartz cladding; HCR is an ultra-pure quartz fiber with "radiation hard" core (high OH content, believed to make it more radiation resistant in the infra-red region) and a plastic cladding; HCP is the same type as HCR but with a low OH content in its quartz core material and HCM are the cheapest fibers in the series (due to a higher level of impurities). The data points represent measurements conducted by averaging peak integral densities from a number of camera images of the fibers' light output on the screen at fixed intervals during the irradiation. Measurement error bars are dominated by fluctuations in the electron beam intensity.

Relatively little or no loss can be seen for the quartz clad fibers, while the PMMA clad fibers lose transmission after approximately 700 Mrad, presumably due to structural damage of the plastic cladding. Damage resistance for all fiber types can be considered as impressive. Depending on the application, one can select a fiber type with sufficient radiation resistance; either a less resistant (and less expensive) plastic clad fiber or a more resistant quartz clad fiber. The basic difference between quartz fibers, assuming a contamination due to impurities kept below the 10 ppm level, is in their cladding material.

3 THE CHERENKOV EFFECT IN OPTICAL FIBERS.

There are three major issues to address when considering the Cherenkov effect in a detector based on quartz optical fibers. First is the light yield caused by the passage of a single charged particle in a fiber. Second is the probability of survival of the emitted photons as the Cherenkov light is created inside the fiber waveguide. This point is controlled by the Numerical Aperture (NA) of the fiber waveguide and by the directionality of the Cherenkov effect. The third issue concerns the application of these points to the specifics of shower development and the choice of the optimal fiber configuration in an absorber for a given application.

The light yield of the Cherenkov effect is given by the formula [16]:

$$\frac{d^2N_{ph}}{dLd\lambda} = 2\pi\alpha z^2 \frac{sin^2\theta_c}{\lambda^2}, \tag{1}$$

where α is the fine structure constant, θ_c is the Cherenkov angle, λ the wavelength and L the path of the particle with charge, z, through the medium. Cherenkov light is emitted along a cone with an angular opening given by:

$$cos\theta_c = \frac{1}{n\beta}, \tag{2}$$

where $\beta = v/c$ and n is the index of refraction of the medium.

The index of refraction of quartz as a function of the wavelength is shown in figure 2. The right scale shows the expected Cherenkov photon yield in quartz per 20 nm bin in wavelength. In this paper we limit our consideration to the interval between 180 and 600 nm, defined by the transmittance of quartz and by the quantum efficiencies of the available photocathodes. In this region, the opening of the Cherenkov cone for β=1 particles is in the interval 46.7° to 50.1°.

As equation (1) indicates, Cherenkov photons are generated in number as $1/\lambda^2$. Single fiber tests [14] have shown that filtering out the UV photons reduces photoelectron statistics to 1/3 of that which would be otherwise obtained. Since this loss can be more than fully recuperated by using fibers with higher NA, tradeoffs can be made between wavelength sensitivities of photon-detectors and fiber candidates.

Fiber light output depends on the direction of the traversing particle because Cherenkov light is radiated along the surface of a cone. Figure 3 schematically shows the geometry of the Cherenkov effect in a cylindrical fiber waveguide. The figure depicts a longitudinal section (point O to O_1) of fiber, of radius R. A particle is shown traversing the fiber, emitting Cherenkov light at point P. The trajectory of the particle with respect to the fiber can be given by α, the angle between the particle's trajectory and the fiber's longitudinal axis and also b, the distance of closest approach between the particle trajectory and the fiber axis (impact parameter). Cherenkov light is emitted from the point P along the surface of a cone with half-angle θ_c. This light intersects the fiber core-cladding interface and is captured or not depending on the intersection angles ξ, ψ and η as defined in the figure.

The condition for capture and transport down the fiber is given by [17]:

$$\xi \geq \xi_{lim} = arcsin\left(\frac{n_{clad}}{n_{core}}\right), \tag{3}$$

where:

$$cos\xi = cos\eta \ sin\psi, \tag{4}$$

and:

$$sin\eta = \frac{\rho}{R} sin\left(arctan\frac{sin\theta_c \ sin\omega}{cos\theta_c \ sin\alpha + cos\omega \ sin\theta_c \ cos\alpha} + arcsin\frac{b}{\rho}\right), \tag{5}$$

and:

$$cos\psi = cos\alpha \ cos\theta_c - sin\alpha \ sin\theta_c \ cos\omega. \tag{6}$$

The distribution of photons trapped inside a fiber, as calculated by equation 3, for Cherenkov photons created by β=1 particles is shown in figure 4 as a function of the impacting particle's angle, α, and impact parameter, b. The peak of the distribution is a wide "fish-tail"-like maximum, positioned between 40° and 50°. The NA of the fiber considered in figure 4 is 0.37, where $NA = \sqrt{n_{core}^2 - n_{clad}^2}$ and is equal to the sine of the nominal limiting exit half-angle for meridional rays (ie. those rays whose paths are confined to a plane which intersects the fiber axis) exiting into air. The "spike" at small angles and large impact parameters is generated by a large number of photons produced by particles traveling almost parallel to the fiber axis, multiplied by a small survival probability. In practice, this particular combination of input parameters (low α, high b) creates only highly "spiralling"

photons that are not easily used. All photons are actually non-meridional and quasi-spiral around the center axis and we define the radius of this quasi-spiral as the distance of closest approach to the fiber's longitudinal axis. We then refer to highly spiralling photons as those photons whose quasi-spiral radius approaches the radius of the fiber itself. The angle, ψ, between their trajectories and the fiber axis can be rather large and as a result they arrive at the end of the fiber with such a high incident angle that the majority of them will be either reflected back into the fiber or will be refracted with such a large exit angle that they are likely to miss the photocathode. The possibility that these photons remain in the fiber at all comes from the fact that they were emitted close to the core-cladding interface.

At low particle momentum, the decrease of β induces a decrease of the Cherenkov angle and a shift of the "fish-tail" towards smaller angles. For β below 0.7, the emitted photons almost coincide with the particle trajectory and therefore only particles which are nearly parallel to a fiber's longitudinal axis will be able to produce light that reaches the end of the fiber.

In a calorimeter all impact parameters, b, are equally likely. Averaging over all impact parameters of distributions like that shown in figure 4 results in distributions of photon survival probability as a function of the incident particle angle, α, as such shown in figure 5. Figure 5(a) corresponds to a NA= 0.22 fiber and figure 5(b) corresponds to a NA = 0.37 fiber. The outer, solid distributions show the probability (per angular bin of 2°) that Cherenkov photons are captured and transported down the fiber. Not all the photons trapped in a fiber will be available outside of the end of the fiber unless perfect optical contact is made between the fiber and a light detector's photocathode. The dashed lines of figure 5 describe the probability that the photons exiting the fiber (into air) are not lost due to total internal reflection at the end surface, taken to be flat and perpendicular to the fiber axis. Of the remaining photons described by the dashed lines, those exiting inside the fiber's nominal exit angle have a higher probability to successfully reach the photocathode. These photons are described by the inner, dotted curve of the figure. This last cut (defined for meridional rays) may be too sharp but it begins to approximate the filtering effect caused by a gap between the fibers' end faces and the light detector's photocathode. Barring wet optical connections, it can be assumed that one is collecting photons between the dashed and dotted distributions, depending on the photon-detector and optical connection being used. All the curves have maxima between 45° and 50°. As a consequence, the probability of photon survival is maximized when the impinging particles cross the fibers at the Cherenkov angle. One should note from figure 5 that a NA=0.37 optical fiber yields roughly four times the number of Cherenkov photons as a NA=0.22 fiber.

We used distributions of Cherenkov photon light yield in optical fibers, as a function of particle speed, incident angle and impact parameter, to create sets of data tables which are applied in our simulations. While the tracking of the showers is performed by GEANT [18], the Cherenkov effect is treated through the use of the light yield data tables, thus reducing the required total CPU time.

These calculations are normalized to measured angular scans of single fibers using the experimental apparatus shown in figure 6. Response to single particles was measured using an 8 GeV electron beam at the CERN PS. Single fibers, 1 meter long, were mounted side-by-

side in a 6 mm wide ribbon and read out at one end by a UV sensitive Hybrid PhotoDiode (HPD) [19, 20, 21] and by a Philips XP2020/Q [21]. Single particles were selected by a set of beam-defining scintillation counters and by two arrays of 1.5 mm diameter scintillating fibers acting as a trigger and veto respectively (see figure 6). Various types of fibers from different manufacturers were tested and results were reported elsewhere [14].

The results of such measurements are photoelectron response distributions which are fit to a function which integrates over the variation of Poissonian probability of light yield (in photoelectrons) produced by particles hitting the fiber with all impact parameters, b. As an example, the results shown in figure 7 give the light output (in photoelectrons) from one meter long, 0.5 mm diameter, CeramOptec NA=0.37, plastic clad (a) and INFOS NA=0.22, quartz clad (b), quartz fibers as a function of incident angle, calculated for impact position zero (incident particle through the fiber axis). The difference between the two fibers' numerical apertures is clearly discernible in the measurements and the solid line shows the simulated behavior normalized to experimental results. One would expect from figure 5 that the photoelectron response peak (at 45°) for the NA=0.37 fiber would be twice that of the NA=0.22 fiber, but the measurement shows that plastic cladding eliminates roughly the same signal (in the UV region) that the larger NA gains overall.

4 SPEED OF RESPONSE AND INHERENT RATE CAPABILITIES.

Cherenkov radiation, a polarization effect, occurs on a much shorter time scale than the propagation of a hadronic shower through a calorimeter. Figure 8 (note the vertical, logarithmic scale and suppressed horizontal zero) shows the velocity distribution for Cherenkov light along the longitudinal axis of an optical fiber waveguide for the three cases mentioned in the discussion of figure 5(b). Solid, dashed and dotted lines in figure 8 refer to the same conditions and line types for figure 5(b). The velocity distribution for Cherenkov photons created by β=1 particles, considering all impact parameters and incoming particle trajectories, and trapped along a fiber with NA = 0.37 is shown in figure 8, solid line. The long tail towards lower velocities is composed of photons which are highly spiralling within the waveguide. Eliminating photons which would be internally reflected at the end face of the fiber results in the dashed line of figure 8. The distribution still has a low velocity component given by a number of highly spiralling photons that have the potential to be refracted out of the fiber end face at angles greater than the nominal exiting angle of the fiber. In a previous section it was stated that these photons would be less easily coupled with a light detector photocathode, given their high refraction angle. The dotted line of figure 8 shows the velocity distribution for photons refracted out of the fiber at angles such that they are still inside the fiber's nominally exiting angle. The low velocity component is reduced to a small shoulder and the full width at half maximum of the distribution is just 0.6 cm/ns. An arrival time distribution for a particle crossing a NA=0.37 optical fiber, one meter from its readout end, is shown in figure 9 for the conditions described by the dashed line of figure 8. At time t=0 ns on the figure the Cherenkov photons were created and the full width at half maximum is just 0.3 ns.

The limiting factor in speed and rate capabilities of the quartz fiber calorimetry technique is the light detector readout technology. The optical signal is combined with the re-

sponse shape of the light detector and with the cable bandpass. Figure 10 shows a typical detector (Proto-2, to be described later) response to a single, 160 GeV, proton shower using a Philips XP2262B PMT, taken with a LeCroy 7200 digital oscilloscope after 10 meters of cable. The delayed or late hadronic energy depositions (proton recoils, γ-neutron capture, γ secondary fission) for dE/dx based calorimeters as reported in reference [22] produce no signal in a quartz fiber calorimeter and so do not affect signal speed. Even in LHC interaction regions, where there will be 25 ns between bunch crossings, no signal processing will be necessary in order to isolate signals from different interaction crossings, thus eliminating effects of the pile-up of previous events. Given a fast light detector, one could foreseeably profit from timing information to assist in vertex detection.

5 APPLICATIONS IN CALORIMETRY.

The features discussed previously apply to the Cherenkov effect of a single particle in a single fiber. When quartz fibers are used as a detection medium in a sampling calorimeter a number of phenomena, different from those of dE/dx based calorimetry, are involved.

Recapitulating the basic characteristics of the Cherenkov effect in a single fiber:

a) The effect has a threshold ($\beta \sim 0.7$) and with the decrease of β the light yield drops quickly.

b) The total light yield for a $\beta = 1$ particle is directly proportional to the length of the trajectory.

c) Particles must cross the fiber within a narrow angular interval (whose maximum is at about 45°) in order to produce a significant signal.

d) The dominant part of the Cherenkov light is emitted in the UV domain (according to equation (1)) and working with UV sensitive photon-detectors will maximize photon statistics.

Point a) is illustrated in figure 11 showing calculated dE/dx and Cherenkov photon yield per 0.1 mm in quartz as a function of particle velocity, β. The threshold of the Cherenkov effect is clearly visible although it is somewhat broad due to the different indices of refraction and photon yields for different wavelengths. The dE/dx of particles in different materials are also shown in order to illustrate some of the fundamental differences between Cherenkov and ionization based calorimetry. For the latter, ionization energy is used as the primary means for observing shower characteristics and is most efficiently sampled in the low β region. The former, relying on Cherenkov radiation, most effectively samples the high β shower particles. While dE/dx increases with the decrease of the particle energy, Cherenkov light production vanishes very quickly. Although the threshold for Cherenkov light production in quartz is $\beta \sim 0.65$ the light production drops rapidly below $\beta = 0.99$. This corresponds to a kinetic energy of 3.1 MeV for electrons, 643 MeV for muons and 850 MeV for pions.

A further consequence of the Cherenkov threshold is the resulting low sensitivity to induced radioactivation of the calorimeter and to the intense flux of low energy neutrons expected to be present in a LHC interaction region, as compared to a dE/dx sensitive calorimeter. In general, particles emitted from decaying nuclei are of low β, and therefore produce little or no Cherenkov signal but are efficiently detected by dE/dx based calorimetry. Neither is there significant Cherenkov radiation from the protons which result from neutron-proton

elastic scattering. The angular distribution of the few fast charged particles from nuclear decays are isotropic and only $\sim 2\%$ of them will be candidates to enter fibers within the angular acceptance necessary to produce a Cherenkov signal. The effect of limited angular acceptance of fibers (see figure 4), together with the threshold effect, makes the QCal technique intrinsically insensitive to radioactivation.

As stated in point b), $\beta > 0.99$ particles have constant light yield per unit length of their trajectory in the medium and the total charged path length in a shower increases with energy. This is one of the fundamental reason that the quartz fiber calorimetry technique may have a linear response as a function of energy. The integrated path length of the hadronic fraction of a shower is smaller than that of EM contributions. But fiber orientation can either enhance or suppress sampling of the long and highly forward path lengths of the hadronic component of a shower. In order to illustrate this effect we performed Monte Carlo simulations where the integrated path length of different components of 100 GeV proton induced showers in a lead absorber were recorded.

Figure 12(a) shows the total charged particles' path lengths (hadronic and electromagnetic), figure 12(b) the path lengths of electrons and positrons, and figure 12(c) of hadrons (mostly pions and kaons) in an infinite lead slab as a function of their velocity, β, and of their angle, α, with respect to the direction of the initial particle (in bins of 2°). For comparison, the path length induced by a 100 GeV electron shower is shown in figure 12(d). The influence of $\beta > 0.99$ particles is dominant in all cases but the angular spread is dramatically different. By 30° in angle, the hadronic component has declined significantly. The EM component largely goes towards the forward hemisphere but a significant fraction even goes backwards. It should be noted that the figure's angular bins are integrated around the azimuthal angle. Thus, a 1° bin around the direction of the incident particle means 115 times smaller solid angle than a 1° bin around $\theta = 90°$. This accounts for the smaller quantity of path lengths in the first bin of figure 12(b) than in the second and third bins (at $0.99 < \beta < 1$), even though the EM component is forward peaked. The integrated path length for the EM component of the hadronic shower is greater than that for the hadronic and the distributions with respect to angle are different. Because shower sampling using the QCal technique is strongly angularly dependent, the relative fractions of path length efficiently sampled for the EM and hadronic components will change depending on which angular orientation (of fiber relative to the original particle direction) is used.

These diagrams are also the basis for a discussion of point c): the angular acceptance of quartz fibers. As previously shown, particles must cross fibers within a narrow angular window oriented around 45° to produce the maximum signal. Fibers parallel to the direction of incoming particles (0°) will most efficiently detect track segments in the 45° angular region of figure 12(a) which, however, is not the most densely populated angular region. Examination of figure 12(c) shows that there are virtually no hadronic track segments remaining in this angular region whereas the EM component (figure 12(b)) is strongly represented. Thus the calorimeter would be much more sensitive to the EM component than the hadronic component. However, if a fiber is tilted at 45° it will be sensitive to those track segments which are in a narrow window around 0° on the figure, sampling both the EM and hadronic components where they are most heavily represented in path length.

Existing simulation programs are optimized for dE/dx based calorimeters. The peculiarities of the Cherenkov effect in optical fibers discussed previously required that a new set of simulation routines had to be developed. Whenever it was possible, we relied on measurements and prototype tests to verify our simulations.

Simulations were done in order to investigate the differences in detector response to electrons and pions for two different geometries and the results are shown in figure 13; for a 45° fiber configuration (a) and for a 0° configuration (b). The simulation used for the 45° configuration has been verified by extensive beam tests while that for the 0° device has not. The simulated 45° geometry consisted of 1 mm diameter quartz fibers distributed in ribbon layers alternated with lead absorber plates for a filling ratio, quartz:lead, of 1:100. The geometry simulated for the 0° calorimeter consisted of the same fiber type, absorber type and filling ratio but with fibers uniformly distributed within the absorber and pointing in the direction of the detector's front face. In order to avoid channeling effects, the simulated 0° calorimeter was tilted at 3° to the incoming particles' trajectories. Dimensions were such as to contain 99% of 1 TeV showers' integrated energy.

Response to electrons and pions is shown in figure 13 (in photoelectrons/GeV) along with their resulting e/π response ratios. Error bars are statistical only and are $\sim 5\%$ for all points. As expected from figures 4 and 12, light yield of the 45° geometry is greater than (roughly two times) that of the 0° geometry in all cases.

We attempted to extract the intrinsic em/h of the two geometries by making a fit to the e/π ratios using the function [23]:

$$\frac{e}{\pi} = \frac{\frac{em}{h}}{1 - F_{\pi^0}(1 - \frac{em}{h})} \ , \tag{7}$$

where e/π is the ratio of the calorimeter's electron to charged pion responses and em/h (the only free fit parameter) is the ratio of the calorimeter's intrinsic response to EM and hadronic shower components. The EM fraction of a hadronic shower was taken to be $F_{\pi^0} = 0.12log(E)$, where E is the initial particle's energy in GeV.

The 45° geometry shows an expected non-unity em/h. $\pi^{\pm}$ contributions are not negligible and lead to an em/h of 1.8 ± 0.1. The 0° geometry, being less sensitive to signal contributions from charged pions has an em/h of 2.5 ± 0.4.

The results show a non-unity compensation but simulations lead us to believe that a different (see section 5.2), optimized detector geometry can achieve an energy resolution constant term for hadrons of $\sim$10%.

5.1 ELECTROMAGNETIC CALORIMETRY.

The prototypes built, simulated and tested so far have had rather different geometrical characteristics which reflect the variables under study. A first quartz fiber electromagnetic calorimeter prototype (called Proto-1) was built and tested in 1991 by the CRN Strasbourg group. It is shown schematically in figure 14. Its dimensions were $5 \times 5 \times 20\,\mathrm{cm}^3$ and it included 1500 1 mm diameter, Ensign-Bickford HCR fibers tilted at 40° with respect to the beam, embedded in a lead matrix with a quartz to lead volume ratio of 1:4. The fibers were extended out of the top of the absorber material to Philips XP2020/Q PMTs (sensitive

to UV light). The calorimeter was longitudinally segmented into two halves, each of which was read out independently. The response of this prototype to 10 and 30 GeV electrons is shown in figure 15 to be Gaussian. We measured about 10 photoelectrons per GeV and an electromagnetic energy resolution $\sigma/E = 24\%/\sqrt{E} \oplus 3\%$.

Although too short for hadronic calorimetry, this 1λ deep prototype was tested with a 200 GeV/nucleon sulfur beam in order to check the validity of our fiber response simulation program. Reliable measurements were possible because the 40° design allows an easy side readout and is therefore insensitive to shower leakage and punch-through. Three measurements were made: without pre-radiator, behind 4 cm of tungsten (1λ for sulfur ions) and behind 8 cm of tungsten. The results and the comparison with the simulation program are shown in figure 16. Light output normalization for simulations was performed once for all three configurations. It can be noted that the agreement is good, and that it improves for the later stages of the shower development. This result gave a first validation of our Monte-Carlo simulations for hadronic showers. Another characteristic measured was the pulse duration: at the ADC input (after cables); it was 10 ns wide at the base line.

Thorough beam tests on Proto-1 verified our simulations. In addition, an effort was made to evaluate photon and sampling limits in the detector's resolution. It was predicted (and later confirmed experimentally) that, even with a 45° geometry, a scattered arrangement of fibers plays a dominant role in degrading the energy resolution constant term. Further prototypes, to be described in the next section, were constructed with fibers arranged in ribbons (sandwiched between plates of absorber material) with no transverse separation between fibers. This arrangement more efficiently uses the active medium, substantially reducing the volume filling ratio of the calorimeter, thereby greatly reducing price for comparable energy resolutions.

5.1.1 BEAM TESTS ON ELECTROMAGNETIC CALORIMETER PROTOTYPES.

A second electromagnetic prototype was built and tested in 1993. As it was historically the third prototype built it was given the name Proto-3 (Proto-2, a hadronic module, will be discussed in a later section). Its outer dimensions are $5 \times 5 \times 20\,\mathrm{cm}^3$. The main objectives were the testing of the ribbon arrangement of fibers inside the lead absorber and to precisely measure the electromagnetic shower size as seen by the QCal technique. The calorimeter was laterally divided into two independent readout channels. Schematic front and side views are shown in figure 17. The fibers (produced by CeramOptec GmbH, Bonn, Germany) were arranged at 45° with respect to the incident particle direction and were 0.5 mm in diameter. The fibers' NA was 0.37 and they consisted of a quartz core with PMMA cladding. Fibers were arranged in single fiber thick ribbons with the fibers touching each other in the transverse direction. The fiber planes were separated by 3 mm flat, lead, absorber sheets which, after the 45° tilt, presented to incoming particles a longitudinal absorber thickness of 4.24 mm. This distance is shorter than 1 radiation length for lead (5.6 mm) ensuring frequent longitudinal sampling of electromagnetic showers.

This arrangement was thoroughly studied with simulations and was predicted to improve the energy resolution over the staggered arrangement. The quasi-uniform lateral distribution of fiber ribbons improves the sampling of the showers in their early stages, where

the core is extremely narrow and dense. The fiber-to-lead volume ratio was about 1:8, considerably lower than for the first EM module (Proto-1). Readout was done using Philips XP2020/Q PMTs after an air core, hexagonal light guide used to homogenize the response of the different parts of the photocathode to different fibers. The line response to 8 GeV electrons hitting the centre of one half-module (right) is shown in figure 18 to be Gaussian. Figure 19 shows the response of the detector to electrons with energy between 5 and 100 GeV to be quite linear. Figure 20 shows the resolution as a function of the electron energy. A fit to the data points gives: $\sigma/E = (35.8 \pm 1.8)\%/\sqrt{E} \oplus (0.40 \pm 0.80)\%$ for the right PM and $\sigma/E = (37.9 \pm 2.1)\%/\sqrt{E} \oplus (0.01 \pm 0.90)\%$ for the left PM. The stochastic term scales as $1/\sqrt{V_{SiO_2} : V_{Pb}}$. Most importantly, these tests have shown that the constant term in electromagnetic energy resolution is removed because of the lateral fiber distribution which makes the detector insensitive to changes in the shower profile.

Beam tests were performed using energies from 5 to 100 GeV on the previously discussed EM prototype, Proto-3, along with two other, similarly constructed prototypes, Proto-4 and Proto-R. The characteristics of these three prototypes are summarized in Table I. The three prototypes were constructed with the same geometrical specifications but, in each case, different types of fiber were used, mainly to measure the influence of the numerical aperture on shower characteristics. The quartz fibers in Proto-3 had a hard polymer cladding (NA=0.37). Those for Proto-4 and Proto-R had silicone cladding (NA=0.40) and fluorinated quartz claddings (NA=0.22) respectively.

The results of beam test for the three prototypes are summarized in Table II. All three prototypes were measured to have EM energy resolution constant terms compatible with 0% and it was observed (using neutral density filters) that the stochastic term had roughly equal contributions from sampling fluctuations and photon statistics. The number of photoelectrons expected from minimum ionizing particles (mips) was computed using single fiber measurements, taking into account core/cladding dimensions and readout quantum efficiencies. The results were compared to the light output measured with 8 GeV muons and found to be in excellent agreement (the signal from δ-rays at this energy is negligible). It is interesting to note that mips deposit only 300 MeV in the detector but produce 0.6 to 0.8 GeV equivalent visible energy in the quartz prototypes, thus showing that calibration of a quartz fiber calorimeter with muons is possible. The calorimeter was also rotated by 180° so that the muons entered from the back and the signal was reduced by a factor of at least 50. This can be an important issue in a collider environment where the beam gas muons are numerous and which impact the detector from the unshielded backside. By contrast, in such an environment, a dE/dx based calorimeter would be equally sensitive to muons regardless of direction.

5.1.2 ELECTROMAGNETIC SHOWER SIZE.

Shower sizes for the quartz fiber calorimetry technique can be measured by performing a scan between the right and left halves of a prototype. The geometrically seamless lateral separation of Proto-3 and Proto-R readouts allowed us to treat each prototype as two separate detectors with no space division between them since each half is large enough for full lateral shower containment. Figure 21 shows the results of a transverse scan along the front

face of Proto-R with 50 GeV electrons. Position information was provided by a multi-wire proportional chamber with 200 μm horizontal and vertical resolution. The signals from each of the two PhotoMultipliers (PM-1 and PM-2) are shown along with their sum, as a function of transverse, horizontal impact position. Such measurements were performed for both of the prototypes and in each case we observed a 5% dip in the response of the calorimeter at the interface between the two readouts which may be caused by a small, transverse gap of dead space between the fiber ribbons or by light collection inefficiencies at the fiber ribbon edge. This dip did not affect other measurements such as energy resolution or the line shape of response for these prototypes since the two, transversely separate readout channels were treated and analyzed as separate detectors.

Figure 22 (clear circles and left axis) shows the results of a transverse scan of Proto-3 with 8 GeV electrons. The response shown is that of one PM subtracted from the response of the other and the solid line is the result of a fit of the data to an arc tangent function. Careful examination of the distribution shows it to be completely symmetric. The same figure shows the electromagnetic lateral shower profile (darkened circles and right, vertical scale) as the derivative of data. The electromagnetic, lateral shower profile can be fitted as a sum of two Gaussian functions, with $\sigma = 0.86$ mm and 3.4 mm, with the two contributions having approximately the same integral. Both terms describe a visible shower size which is far below a Molière radius (12 mm for lead). Narrower shower sizes were measured for Proto-R, whose fibers have a smaller NA. Detailed simulations have shown that the basic reasons for the difference in shower sizes between dE/dx based calorimeters and quartz fiber calorimeters lies in the different kinds of signal-generating particles for the two techniques and in the very limited angular acceptance of the quartz fibers. Figure 23 summarizes measurements done using Proto-3 and Proto-R with 8 and 50 GeV electrons.

Advantages of Cherenkov effect based EM calorimeters include high radiation tolerance, shorter pulses, greatly reduced visible shower sizes and a energy resolution constant term measured to be compatible with 0%.

5.2 HADRONIC CALORIMETRY.

Hadronic shower measurement is less limited by sampling fluctuations than that for electromagnetic showers but sampling still plays some role in hadronic energy resolution. As in the EM case, geometries in which matrixing of fibers leads to transverse separations in the active medium are inferior to a layered ribbon geometry. Measurements were performed on a coarse, matrixed fiber, hadronic prototype which was built and tested in 1992 by the INFN Torino and CRN Strasbourg groups, as a first prototype for the zero degree calorimeter of experiment NA50 [1, 4, 5, 6, 10]. For this application in heavy ion physics, the energy of the projectiles is so great (160 GeV/nucleon resulting in up to 33 TeV lead projectiles) that sampling fluctuations virtually cease to play a role. As it was historically the second prototype built, we refer to this module as Proto-2.

5.2.1 BEAM TESTS ON A HADRONIC CALORIMETER PROTOTYPE.

An objective in measuring the characteristics of the calorimeter prototype, Proto-2, was to verify that the set of Monte Carlo simulations that we had developed were accurate enough to reliably reproduce response to hadronic showers. The dimensions of the prototype

were $22 \times 22 \times 90\,\mathrm{cm}^3$, sufficient for a containment of more than 90% of heavy ion (S^{32}) showers. It was longitudinally segmented into four blocks each read out by four PMTs. Figure 24(a) shows a sketch of Proto-2. The fibers were arranged inside the lead in four interleaved patterns, as shown in figure 24(b), with each matrix read out by a separate PMT. The distance between fibers within one matrix was 3.7 mm transversely and 12.44 mm in the longitudinal direction. The total fiber-to-lead filling ratio, when using all four sets of PMTs, was 1:10. By analyzing the response of different combinations of PMTs, we could check the resolution for a volume ratio of 1/40, 1/20, 1/13.3 and 1/10. Also, different PMT combinations allowed us to check different fiber distributions. The fibers embedded in the lead were 1 mm diameter HCR quartz fibers (produced by Ensign Bickford) with a numerical aperture of 0.37. To reduce cost, the connection between the quartz fibers and the PMTs was made with 1mm diameter, NA=0.6, Mitsubishi plastic fibers made of PMMA (so all UV light was lost). The PMTs (Philips type XP2262B) had ordinary glass window and type S photocathodes.

A first set of tests were performed in April 1992 with 6.4 TeV sulfur ions. The attained response distributions were visibly non-Gaussian for low volume fiber ratios, with the shape improving for the highest fiber ratios. Figure 25 shows the measured resolution compared with simulations. Using only 2 PMs per block, we have two different fiber readout combinations (PM-1 and PM-3 or PM-1 and PM-2); slightly better resolution is obtained when the fiber distribution approaches layers in the transverse direction (PM-1 and PM-2, better sampling of the density profile of particles in the shower). Despite the fact that tests performed with a single energy projectile couldn't be used for a detailed study of the calorimeter resolution as a function of energy, the energy of the projectiles was so high that the obtained resolution was dominated by the constant term giving the limit of this calorimeter's performance. The difference between the resolutions of two different fiber distributions corresponding to readout of the same fiber density was the first experimental indication that the fiber distribution is important also for hadronic showers.

Another set of tests was performed in June 1994, with pions and electrons. Figure 26(a) shows the response of the prototype for pions as a function of their energy, where the error bars are largely inside of the data markers. Detector response shows an expected (due to the Cherenkov signal cutoff) non-linearity towards lower energy showers. The fitted resolution (figure 26(b)) was measured to be: $RMS/E = (208 \pm 9)\%/\sqrt{E} + (8 \pm 1)\%$. Because of the short longitudinal depth of the calorimeter prototype a scintillator plate placed behind the calorimeter during the beam test was used in the analysis to separate events whose showers developed late and leaked from the calorimeter. The calorimeter was too short and too coarse for optimum hadronic resolution, but it proved to be extremely useful in the fine tuning of simulations. The resolution was within limits foreseen by the simulations. The large lateral distance between fibers combined with this calorimetry technique's very small shower size did not allow for meaningful EM shower measurements using this prototype, except for a confirmation that the response distribution for electrons should have two peaks, the higher one corresponding to the events where the initial electron hit a longitudinal layer of fibers and the lower one when the shower core went between the fibers.

To optimize the design of a future hadronic prototype a simulation study was done

and figure 27 shows what we expect in terms of hadronic energy resolution constant and stochastic terms. A hadronic energy resolution of $\sigma/E = 100\%/\sqrt{E} \oplus 10\%$ is expected through construction of a 45° prototype with 200 μm fibers (thinner fibers reduce the price of the calorimeter while keeping the sampling frequency acceptable) in ribbons sandwiched between flat copper absorber plates.

5.2.2 HADRONIC SHOWER SIZE.

To measure the width of the hadronic showers as seen by the QCal technique, an edge scan of the hadronic calorimeter, Proto-2, was performed with 160 GeV protons. Lead was placed at the calorimeter edge in order to let the shower develop uniformly both inside and outside of the calorimeter. Figure 28 shows the result and a comparison with simulations. The simulation agrees, in all respects, with the experimental data for this prototype. Another simulation was conducted in which the longitudinal length of Proto-2 is extended infinitely for complete shower containment. Figure 29 shows the simulated transverse, visible shower shape of the calorimeter as a function of horizontal position of the impinging particle for both 160 GeV pions (figure 29(a)) and 160 GeV electrons (figure 29(b)). As a comparison, the results from an RD25 simulation (previously shown to be in good agreement with experimental results) of a scintillating fiber based calorimetry technique [24] is also shown. The transverse, visible, hadronic shower size of the quartz fiber calorimeter is approximately three times narrower than in conventional, ionization based calorimeters: the quartz fiber calorimeter works as a shower core detector. One of the consequences of this is that the energy of a hadronic shower can be reliably measured very close to the calorimeter edge. The technique's small shower size, radiation hardness and high rate capabilities mean that the calorimeter can operate well even immediately adjacent to a beam tube, thus extending the pseudorapidity coverage to limits unattainable by dE/dx based calorimetry techniques [15].

6 CONCLUSIONS.

We have presented results of extensive prototype studies and detailed simulations which demonstrate the fundamental operating principles and basic properties of a new kind of sampling calorimetry. In sampling calorimetry using Cherenkov effect radiation in quartz optical fibers, the effects of the directionality of Cherenkov emission and the angular selectivity of propagation modes in optical fibers combine to produce a new sampling mechanism with startling properties.

This aspect of quartz fiber calorimetry makes it unique in that that the limited angular acceptance produces very narrow electromagnetic and hadronic showers. Electromagnetic and hadronic showers are about three times narrower (for 90% containment) in a quartz fiber calorimeter than in an ionization based calorimeter. This has the effect of sharply increasing the fiducial volume near beam pipes or other edges and enabling jet separation in a crowded environment.

Because the basic mechanism is the detection of Cherenkov radiation, the calorimeter is intrinsically fast. The signal speed and dead time are limited only by the photon-detector. With no special precautions, a hadronic prototype exhibits a 15ns baseline-to-baseline signal through a phototube in a beam test. In addition, because of the selective propagation modes

in the fiber, the signal time dispersion is small - so small that 0.1ns time resolutions can be attained.

Signal threshold and limited acceptance strongly suppress "noise" from the induced radioactivity of the calorimeter material itself. This will be an important advantage for any high intensity application. The origins of this suppression are threefold. First, no direct signal is generated for low energy, uncharged particles, such as gammas and neutrons. Second, the Cherenkov velocity threshold in quartz requires a particle to have a velocity of about 0.65 of the velocity of light. In practice, this restricts nuclear decay products to be electrons in order to have any chance of being relativistic. Nuclear decays which emit alpha's are invisible, as are all but the most energetic neutron-proton collisions. Compton electrons from γ-e scattering can generate a signal, but must have a minimum of 0.7 MeV to generate light. Third, the angular acceptance of the sampling mechanism amounts to about 2% of 4π steradians. There is an additional suppression factor of 50 from this source alone. Thus, the device is blind to low energy neutrons, and nearly blind to radioactivation.

Clearly, a calorimeter can be constructed from any clear optical fiber, but the use of quartz fibers enables the device to function after Gigarad exposures. This, together with the narrow shower characteristic, opens the possibility of obtaining reliable measurements right up to the edge of the beam pipe in collider experiments. At the LHC, it seems feasible to instrument up to the pseudorapidity of 8, and possibly further, making, for example, a very small angle luminosity monitor credible.

Electromagnetic prototypes were measured to have energy resolution constant terms compatible with 0%, an important quality for precision EM calorimetry at higher energies.

7 ACKNOWLEDGEMENTS.

The authors wish to express their indebtedness to the technical expertise of D. Brozzi of the CERN PPE Division and R. Glassmann of CRN Strasbourg, France. Thanks are expressed to M. Toulemonde and the CIRIL group, CAEN, France, for their assistance in radiation damage tests on quartz samples done at GANIL, to A. Strasser and F. Kunz of CRN Strasbourg, France for assistance with fiber irradiations and to C. Fuchs of the PHASE group, CRN, Strasbourg, France, for help with spectrophotometer measurements of damaged samples. Prototype construction was financed, in part, by INFN, Italy (CPF2 Experiment). The Florida State University group owes thanks for financial support to the United States Department of Energy (grant number DE-FG05-87ER40319). We thank the CERN RD25 collaboration for providing lead used in many of our prototypes. Support for development of this technique from the LAA project and its project leader, A. Zichichi, is acknowledged. Special thanks and deep appreciation are owed to the CERN PS and SPS machine groups without whose help this work would not have been possible.

References

[1] CERN-SPSLC-91-55 (91/10,rec Nov.).

[2] G. Stevenson, Proceedings of the "Large Hadron Collider Workshop", Aachen 4-9 October 1990, CERN 90-10, volume III, pp. 302 and 566.

[3] B. Grosdidier Doctoral Thesis, CRN 92-45, 10 July, 1992.

[4] C. Baglin et al., IEEE NSS, Orlando, USA, 1992.

[5] P. Gorodetzky et al., *Radiation Physics and Chemistry*, (Pergamon Press, Oxford, U.K.) **41** nos. 1/2, (1992) p. 253, eds. R. Clough and K.F. Johnson.

[6] D. Lazic Doctoral Thesis, CRN 93-38, 28 May, 1993.

[7] K.F. Johnson et al., *Proceedings of the Fourth International Conference on Calorimetry in High Energy Physics*, (World Scientific Pub. Co., Singapore, 1994) pp. 438-442, eds. A. Menzione and A. Scribano.

[8] P. Gorodetzky et al., *Proceedings of the Fourth International Conference on Calorimetry in High Energy Physics*, (World Scientific Pub. Co., Singapore, 1994) pp. 433-437, eds. A. Menzione and A. Scribano.

[9] P. Gorodetzky et al., *Proceedings of the Fourth International Conference on Calorimetry in High Energy Physics*, (World Scientific Pub. Co., Singapore, 1994) pp. 462-466, eds. A. Menzione and A. Scribano.

[10] A. Musso et al., *Proceedings of the Fourth International Conference on Calorimetry in High Energy Physics*, (World Scientific Pub. Co., Singapore, 1994) pp. 457-461, eds. A. Menzione and A. Scribano.

[11] A. Contin et al., CERN/DRDC/94-4, January 5, 1994.

[12] G. Anzivino et al., NIM **A357** (1995) 380-385.

[13] V. Gavrilov et al., *Proceedings of the 6th Pisa Meeting on Advanced Detectors*, Elba, Italy, May 22-28, 1994.

[14] A. Contin et al., NIM **A357** (1995) 369-379.

[15] B. Christie et al., RHIC note 13, STAR note 175, Brookhaven, May 13th, 1994.

[16] J.V. Jelley, "Cherenkov Radiation and its Applications," Pergamon Press, 1958.

[17] Erratum: Equation (5) as it is printed in reference [6], page 41, equation 2.4, contains a typing error. Equation (5) given in this text is correct.

[18] Application Software Group CERN/CN, CERN Program Library Long Writeup W5013, March 1994.

[19] R. DeSalvo et al., NIM **A315** (1992) 375.

[20] H. Arnaudon et al., NIM **A342** (1994) 558.

[21] R. DeSalvo et al., *Proceedings of the Fourth International Conference on Calorimetry in High Energy Physics*, (World Scientific Pub. Co., Singapore, 1994) pp. 78-82, eds. A. Menzione and A. Scribano.

[22] A. Caldwell et al., NIM **A330** (1993) 389.

[23] D. Acosta et al. NIM **A308** (1991) 481-508.

[24] M. Mondardini et al., *Proceedings of the 6th Pisa Meeting on Advanced Detectors*, Elba, Italy, May 22-28, 1994, submitted to NIM.

TABLE CAPTIONS

Table I: Electromagnetic prototypes' characteristics. All prototypes were constructed with the same geometry using different fiber types.

Table II: Experimental results for electromagnetic prototypes. Resolutions shown were fit in quadrature for electron energies ranging from 5 to 100 GeV.

FIGURE CAPTIONS

Fig. 1 : Integrated light yield for different kinds of quartz fibers as a function of delivered dose. HCG (darkened triangles) is an ultra-pure (impurities below the ppm level) quartz fiber with a fluorinated quartz cladding; HCR (clear triangles) is an ultra-pure quartz fiber with high OH content core (known to make it more radiation resistant in the infra-red region) and plastic cladding; HCP (clear circles) is the same type as HCR but with a low OH content core material and HCM (dark circles and clear squares) are the cheapest fibers in the series (due to a higher level of impurities).

Fig. 2 : Index of refraction (left scale) of quartz as a function of wavelength shown along with the photon yield (right scale) for a particle crossing 1 mm of quartz.

Fig. 3 : A schematic view of the Cherenkov effect in a step index optical fiber. A photon emitted at the point P travels along the Cherenkov cone and hits the interface core-cladding at point A. **(a)** Three-dimensional view; **(b)** Blow up view of the point of impact of a light ray on the interface core-cladding; **(c)** Projection into a plane perpendicular to the fiber axis.

Fig. 4 : Distribution of the number of photons that exit the fiber (ϕ = 1 mm, NA = 0.37) as a function of the impact parameter, b, and the incident angle, α, of the particle trajectory for a $\beta = 1$ particle. Reflections from the front surface of the fiber are taken into account (no optical contact with a photon-detector). The wavelength distribution of the produced photons is folded with the "nominal" quantum efficiency of a Philips XP2020/Q photocathode.

Fig. 5 : Photon survival probability for fiber with NA = 0.22 **(a)** and for fiber with NA = 0.37 **(b)**. Data is averaged over all impact parameters. The outer, solid lines show the probability that Cherenkov photons created by a $\beta = 1$ particle are captured inside the fiber. The dashed lines show the probability for these photons to exit the fiber successfully (without being internally reflected at the end face) and the inner dotted lines show the probability that these remaining photons refract out of the end face at an angle less than or equal to the nominal exit angle of the fiber (eliminating highly spiralling ones).

Fig. 6 : Schematic view of the set-up for the single fiber Cherenkov light output measurements: S1 = scintillation counter, SV = veto counter, SF = finger counter, BC = multi wire proportional chamber, FV = scintillating fiber veto, FT = scintillating fiber trigger, F = quartz fiber layer under measurement.

Fig. 7 : Results of two angular scans measuring fiber Cherenkov light output (in photo-electrons at impact parameter = 0) for two fibers: **(a)** 500 μm diameter quartz fiber with hard polymer cladding from CeramOptec (NA=0.37); **(b)** 500 μm diameter quartz fiber with quartz cladding from INFOS (NA=0.22). The solid lines show numerically generated, experimentally normalized approximations used for simulations of detectors containing these fibers.

Fig. 8 : Propagation velocity of Cherenkov radiation along a NA=0.37 optical fiber's axis, averaged over all impact parameters and incoming particle trajectories. Solid lines: all photons within the waveguide that manage to reach the fiber end face.

Dashed lines: only photons which are not internally reflected from the fiber end face. Dotted lines: only photons which refract out of the fiber but remain within the fiber's nominal exit angle.

Fig. 9 : Time dispersion of Cherenkov light , after a 1 meter length of fiber, for all photons which exit the fiber end face (same condition as for the dashed line case of figure 8).

Fig. 10 : Digital oscilloscope plot of the detector response for Proto-2 (after 10 meters of cable) to a 160 GeV pion shower using a Philips XP2262B PMT readout.

Fig. 11 : Change in energy deposition per unit length of quartz fiber as a function of incident particle velocity for various absorber materials. Cherenkov light yield, in photons per 0.1 mm of quartz, is also shown (right axis label).

Fig. 12 : Integrated path length, in cm, of different components of a 100 GeV proton induced shower in an infinite slab of lead as a function of their velocity, β, and angle with respect to the incoming particle, α. **(a)** Total charged particles' path lengths (hadronic and electromagnetic). **(b)** Path lengths of electrons and positrons. **(c)** Path lengths of hadrons (mainly pions and kaons). For comparison, the path lengths induced by a 100 GeV electron shower is also shown **(d)**.

Fig. 13 : Simulated electron and pion response in photoelectrons/GeV for two different calorimeter geometries, 45° **(a)** and 0° **(b)**. The e/π ratios for both simulated detectors are shown and the em/h ratio is calculated as described in the text.

Fig. 14 : Schematic view of the QCal electromagnetic prototype, Proto-1. **(a)** Front view showing the fibers exiting the top of the module, being bundled together and fed directly to longitudinally separate readout PMs. **(b)** Side view showing the 40° angle geometry and blow up showing fashion in which fibers were set inside the lead absorber material.

Fig. 15 : Line shape responses of the first prototype to 10 and 30 GeV electrons.

Fig. 16 : Comparison between the measured (solid lines) and simulated (dashed lines) signal distributions of Proto-1. The horizontal scale is the number of photoelectrons and the vertical is the number of events per bin. Zero, four and eight cm of tungsten were put in front of the module. The beam was 200 GeV/nucleon Sulphur ions. PM-1 and PM-2 readout the upstream and downstream half of the module respectively.

Fig. 17 : Schematic front **(a)** and side **(b)** views of electromagnetic prototype, Proto-3. It differs from Proto-1 in that fibers were arranged in ribbons with no transverse space in between. Fibers exiting the top of the detector, are bundled together and fed to transversely separate readout PMs via hexagonal, air core light guides whose lengths were matched to the fibers' numerical aperture for optimal light mixing. The absorber layers consisted of flat lead plates, 3mm in thickness.

Fig. 18 : Signal line shape of the response of Proto-3 to 8 GeV electrons.

Fig. 19 : Response of the EM prototype, Proto-3, to electrons of energy from 5 to 100 GeV.

Fig. 20 : Electromagnetic energy resolution of Proto-3 (clear circles for PM-1 and darkened circles for PM-2) as a function of $1/\sqrt{E}$ together with the data from Monte Carlo

simulation (stars). Due to the improved fiber distribution scheme, the constant term of the fit for Proto-3 is compatible with zero.

Fig. 21 : Detector response as a function of horizontal impacting position of 50 GeV electrons for Proto-R. The separate readout channels are shown (PM-1 clear circles, PM-2 clear squares) along with the sum of the two (darkened circles). The horizontal axis has an arbitrary zero which does not correspond to the detector transverse center.

Fig. 22 : Edge scan (clear circles and left, vertical axis) of Proto-3, measured using a CERN PS 8 GeV electron beam. The edge position is at $x = 2.2$ mm. The solid line is an arc tangent fit to the data. Also shown is the electromagnetic lateral shower profile for Proto-3 (darkened circles and right, vertical axis). The solid line is the result of a fit to the sum of two Gaussians as described in the text.

Fig. 23 : Summary of electromagnetic shower widths of Proto-3 and Proto-R, for various integrated energy containments and for two energies, 8 and 50 GeV.

Fig. 24 : **(a)** Lateral view of Proto-2. **(b)** Distribution of the fibers in Proto-2. The fibers within each block were connected to four different PMTs. By reading different combinations of the PMTs, the response of the calorimeter to different fiber densities and distributions could be obtained.

Fig. 25 : The measured (with S^{32} ions, 200 GeV/n) and simulated hadronic resolution for Proto-2, as a function of the fiber density (i.e. number of PM per block). The large error bars for the simulated events arise from low statistics (only 100 events corresponding to 170 hours of CPU time on a IBM 3090). Experiment errors are inside of the data point markers. See text for the difference between the two different kind of data points.

Fig. 26 : Proto-2 calorimeter response **(a)** and energy resolution **(b)** as a function of pion beam energy.

Fig. 27 : Results of simulations done in order to predict hadronic energy resolution constant terms (darkened squares) and stochastic terms (darkened circles) for various copper absorber plate thicknesses using $200\mu m$ diameter quartz fiber ribbons with a 45° geometry.

Fig. 28 : Edge scan of Proto-2 using 160 GeV protons. The solid line is the result of a Monte Carlo simulation showing good agreement with the experimental data points.

Fig. 29 : Simulated shower shape of Proto-2 (clear circles) using 160 GeV pions **(a)** and 160 GeV electrons **(b)**. For comparison, results from a simulated ionization based, spaghetti calorimeter is also shown (darkened circles) and shower widths for 90% integrated energy shower containment for the two techniques are specified.

Table I. Electromagnetic prototypes' characteristics.

	Proto-3	Proto-4	Proto-R
Fiber manufacturer	CeramOptec	CeramOptec	INFOS
Core ϕ [μm]	500	500	500
Cladding ϕ [μm]	540 (HC)	550 (Silicone)	530 (Q(F))
Coating ϕ [μm]		600 (Acrilate)	560 (Polyimide)
Nominal NA	0.37	0.40	0.22
$V_{\rm Q}/V_{\rm absorber}$	1/8.3	1/9.2	1/8.6

Table II. Results of the electromagnetic prototypes.

		Proto-3	Proto-4	Proto-R
$\sigma(E)/E$	a	$(35.6 \pm 0.2)\%$	$(41.7 \pm 0.3)\%$	$(42.3 \pm 0.7)\%$
$\left(\frac{\sigma(E)}{E} = \sqrt{\frac{a^2}{E} + b^2}\right)$	b	$(0 \pm 0.4)\%$	$(0.7 \pm 0.6)\%$	$(0 \pm 1.1)\%$
$N_{p.e.}$/mip	(UV+Visible)	9.0 ± 0.6	9.9 ± 0.6	12.6 ± 1.0
GeV/mip		0.57 ± 0.06	0.78 ± 0.08	0.78 ± 0.08
$N_{p.e.}$/GeV (electrons)	(UV+Visible)	15.9 ± 1.6	12.8 ± 1.5	16.3 ± 1.7
pC/GeV		2.113 ± 0.002	1.671 ± 0.001	1.675 ± 0.001
pC/mip		1.20 ± 0.012	1.30 ± 0.13	1.30 ± 0.13
Contributions to the stochastic term:				
Photon statistics		$(25.1 \pm 2.5)\%$	$(28.0 \pm 3.2)\%$	$(24.8 \pm 2.5)\%$
Sampling fluctuations		$(26.6 \pm 6.7)\%$	$(31.1 \pm 8.2)\%$	$(34.3 \pm 5.1)\%$

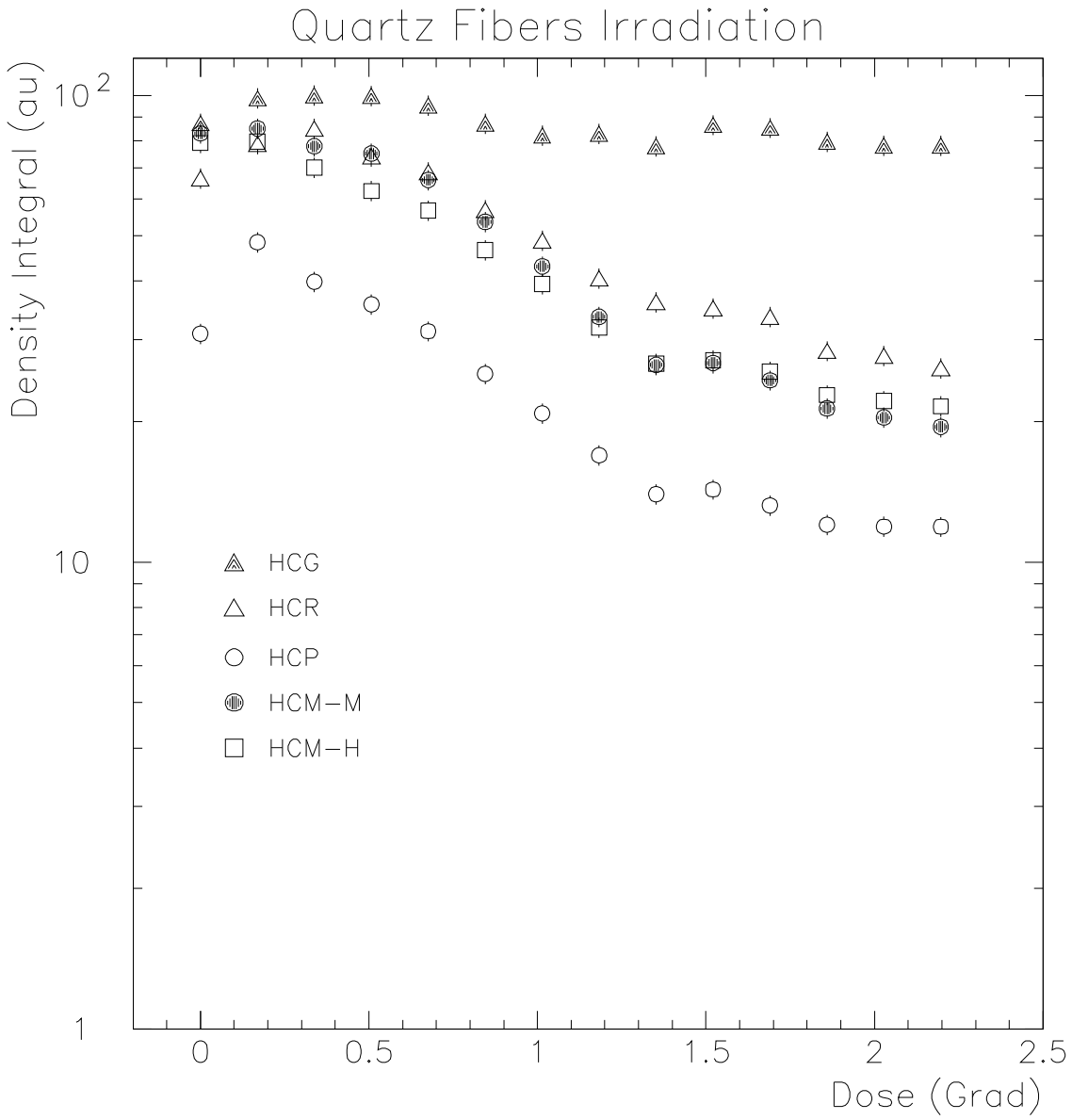
Quartz Fibers Irradiation
Density Integral (au)
10^2
10
1
0
0.5
1
1.5
2
2.5
Dose (Grad)
HCG
HCR
HCP
HCM−M
HCM−H

Figure 1

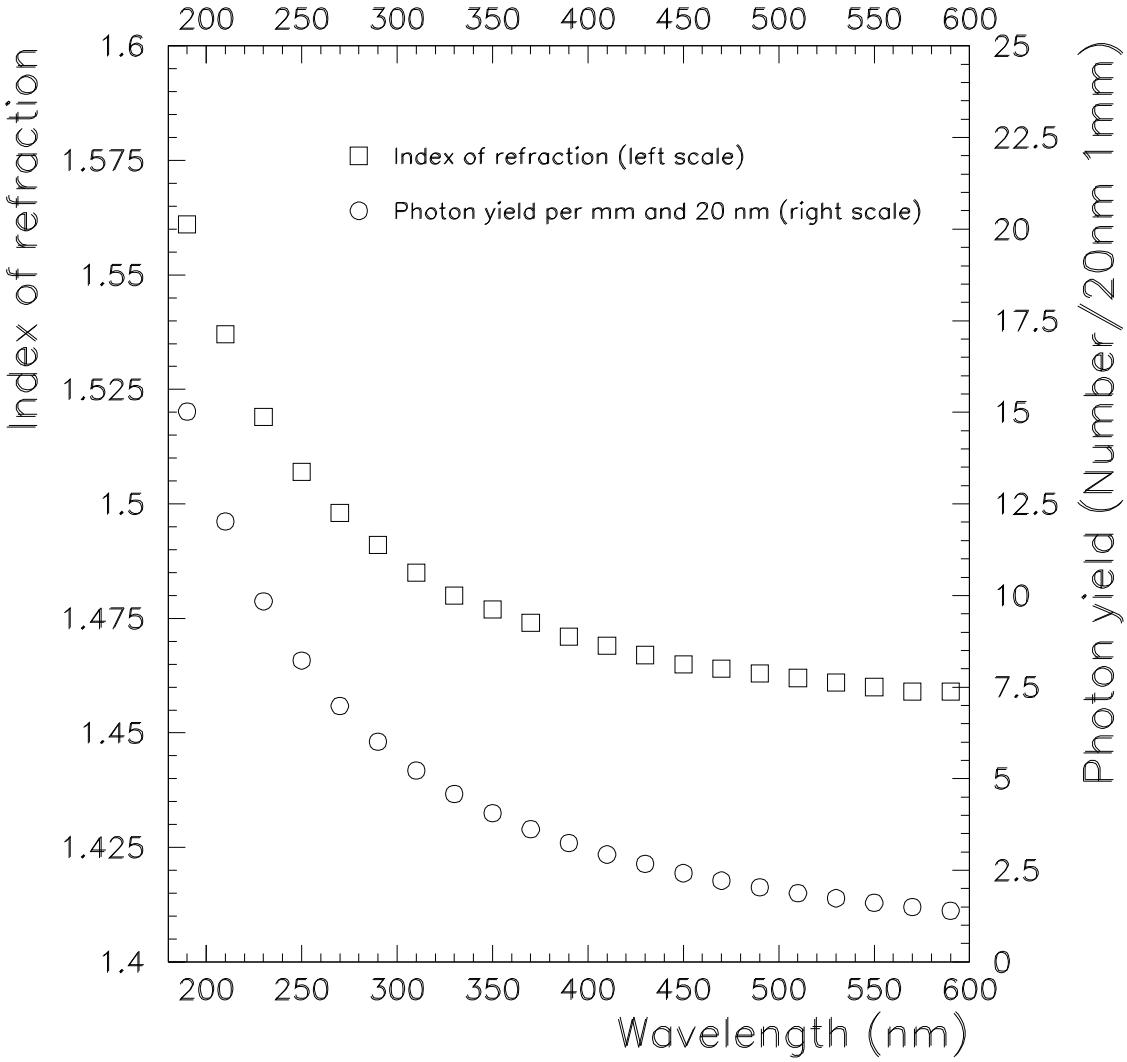
Index of refraction (left scale)
Photon yield per mm and 20 nm (right scale)
Index of refraction
Photon yield (Number/20nm 1mm)
Wavelength (nm)
200 250 300 350 400 450 500 550 600
1.6 1.575 1.55 1.525 1.5 1.475 1.45 1.425 1.4
25 22.5 20 17.5 15 12.5 10 7.5 5 2.5 0

Figure 2

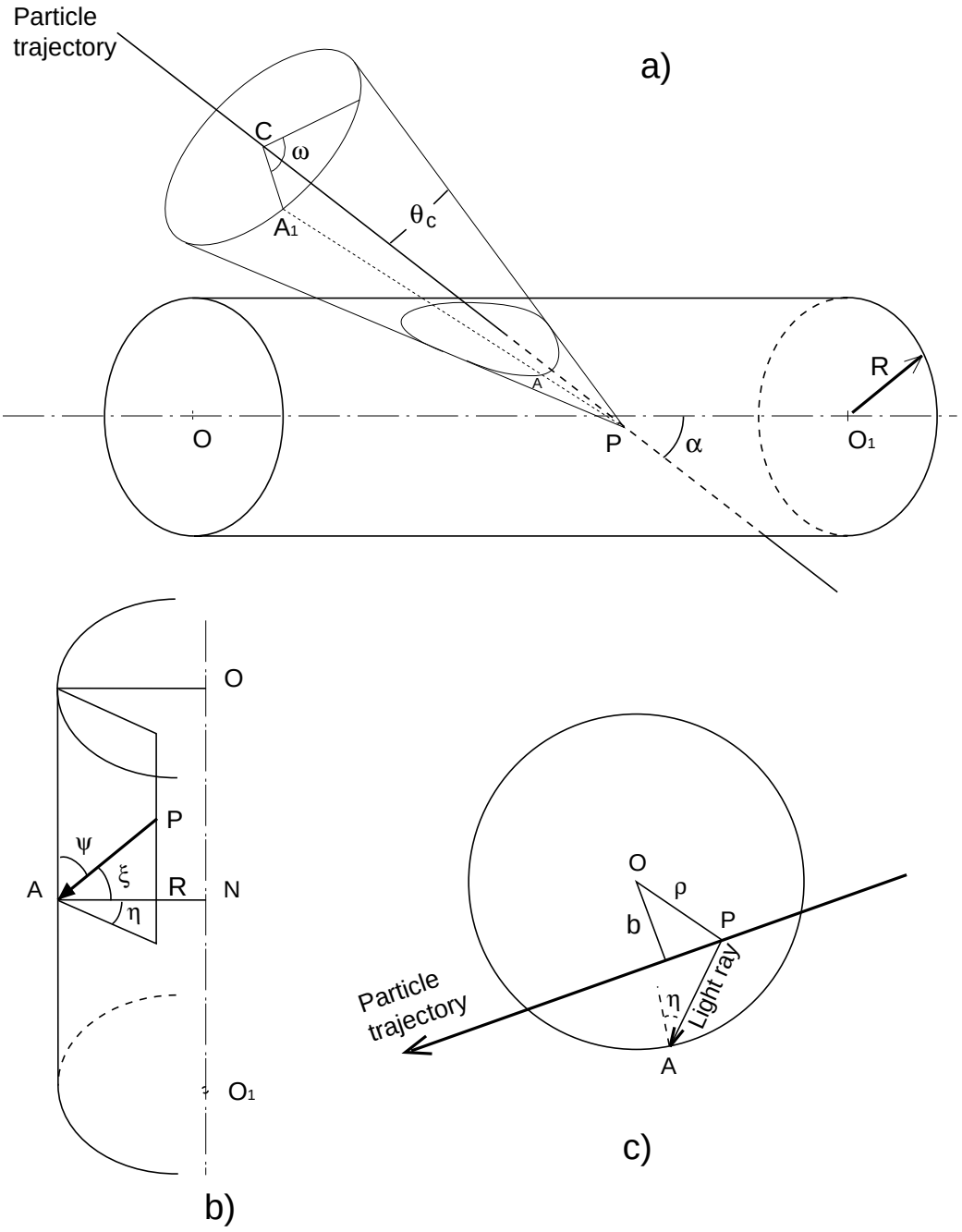
Particle
trajectory
a)
C
ω
θc
A1
A
R
O
P
α
O1
O
P
ψ
ξ
A
R
N
η
O1
b)
O
ρ
b
P
Particle
trajectory
η
Light ray
A
c)

Figure 3

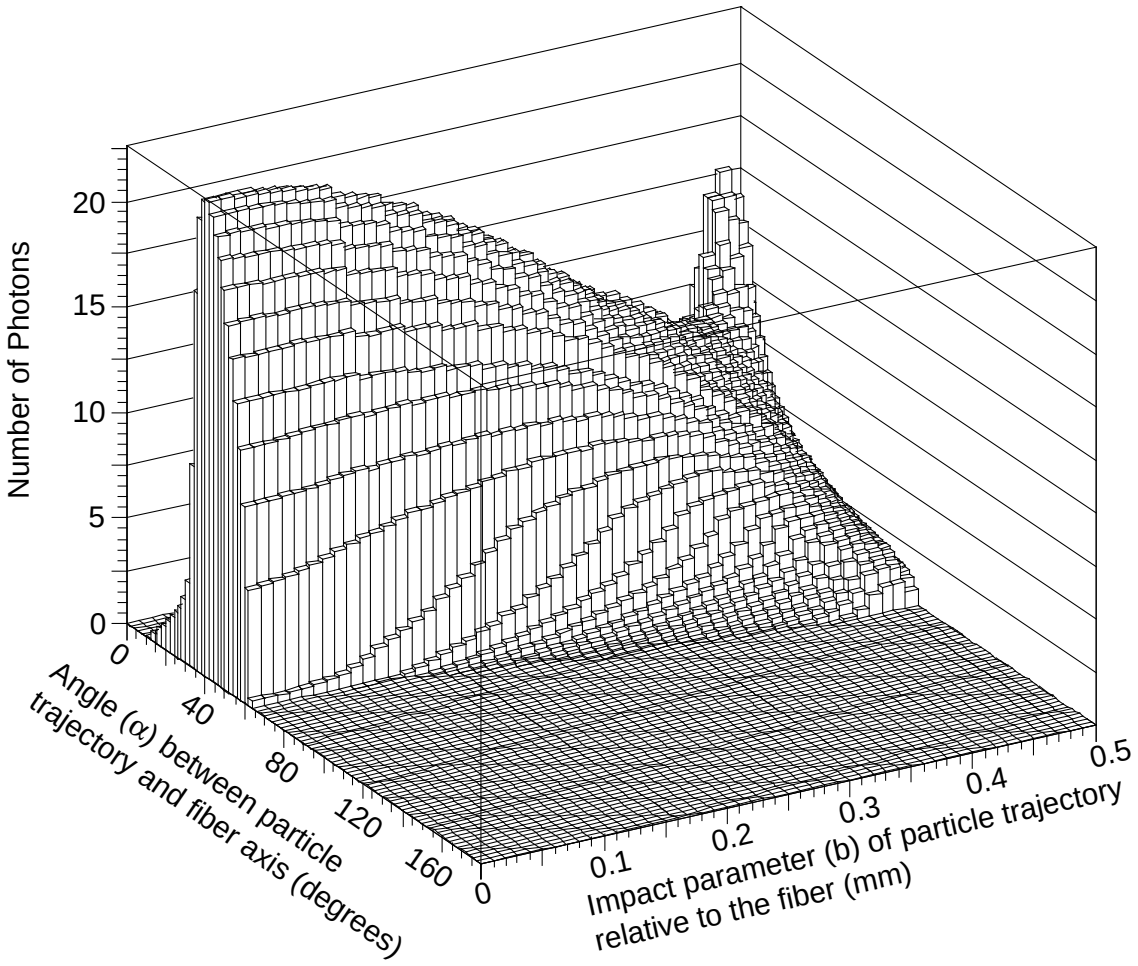
Number of Photons
0
5
10
15
20
Angle (α) between particle trajectory and fiber axis (degrees)
0
40
80
120
160
Impact parameter (b) of particle trajectory relative to the fiber (mm)
0
0.1
0.2
0.3
0.4
0.5

Figure 4

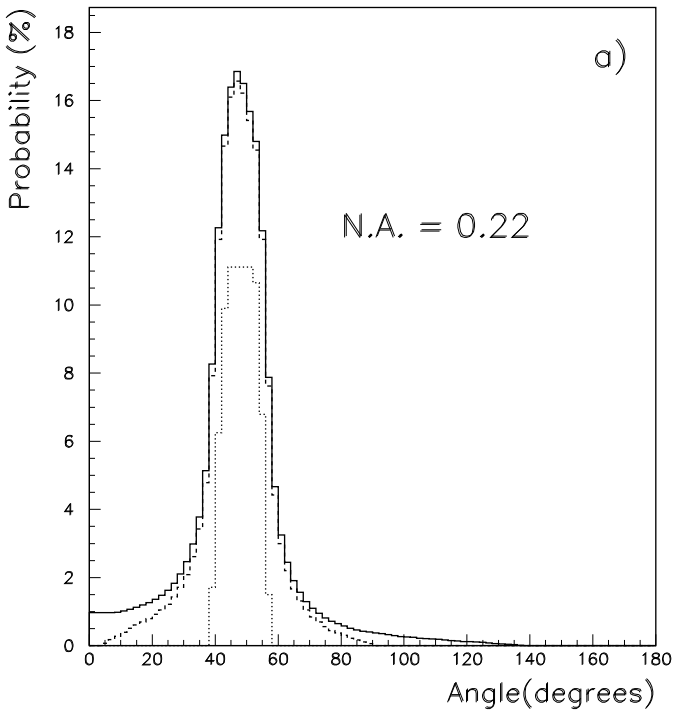
a)
N.A. = 0.22
Probability (%)
Angle(degrees)
0
2
4
6
8
10
12
14
16
18
0
20
40
60
80
100
120
140
160
180

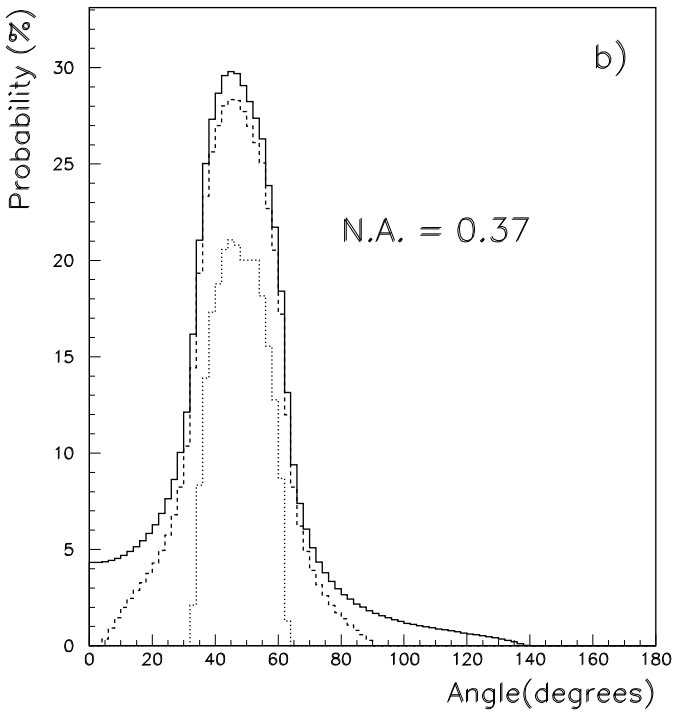
b)
N.A. = 0.37
Probability (%)
Angle(degrees)
0
5
10
15
20
25
30
0
20
40
60
80
100
120
140
160
180

Figure 5

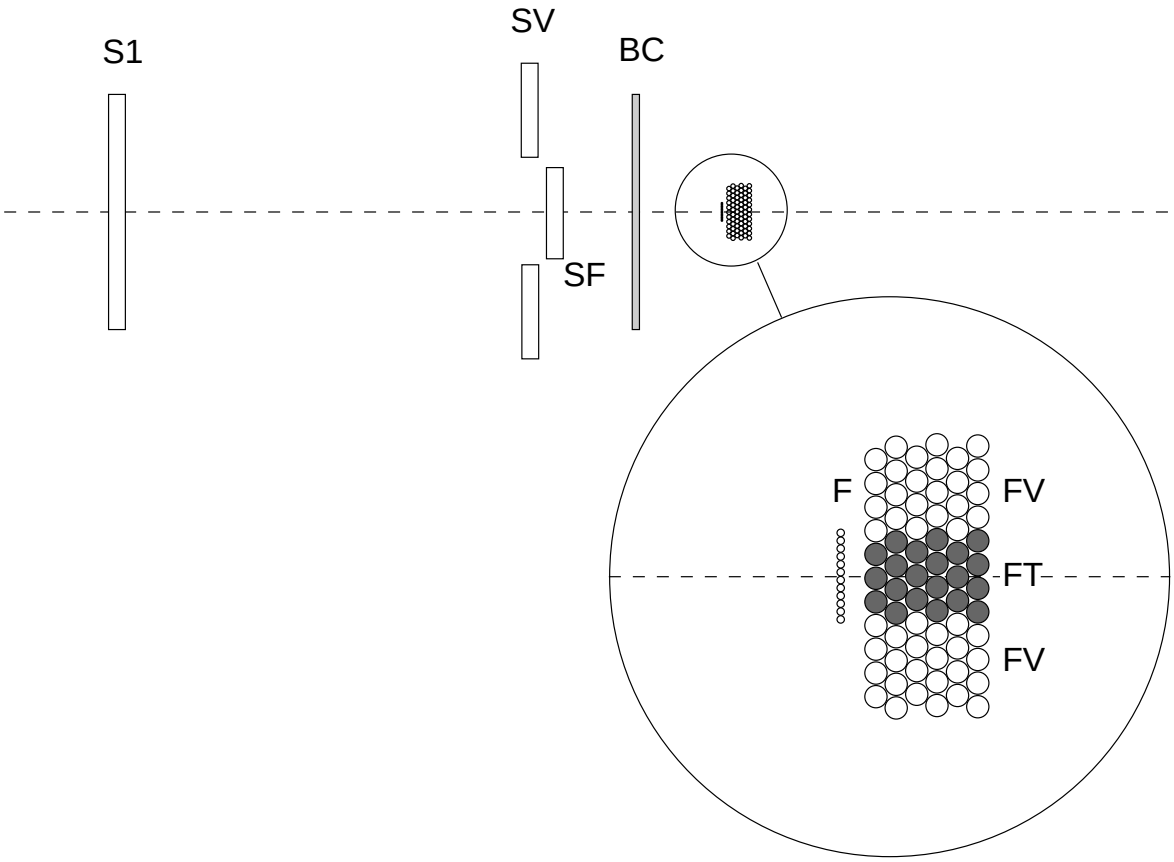

Figure 6

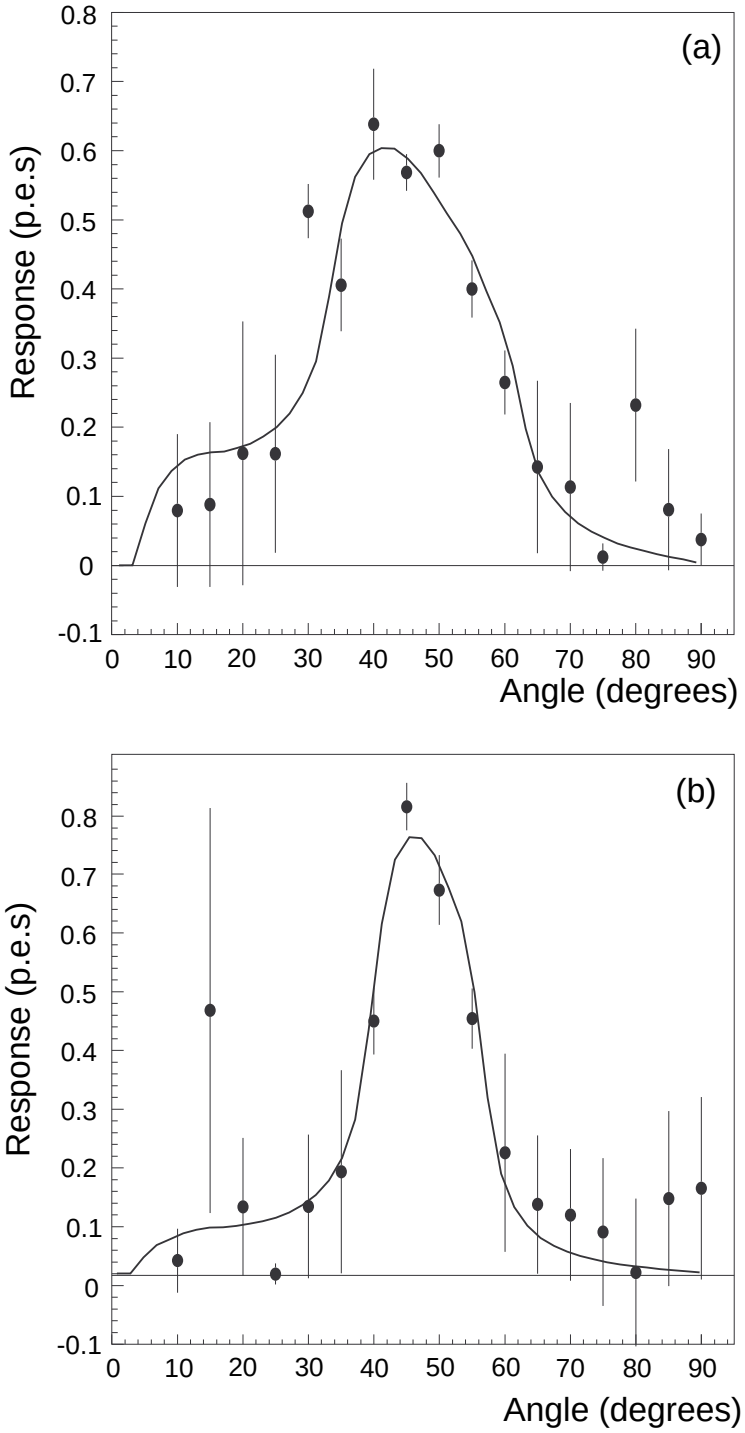

Figure 7

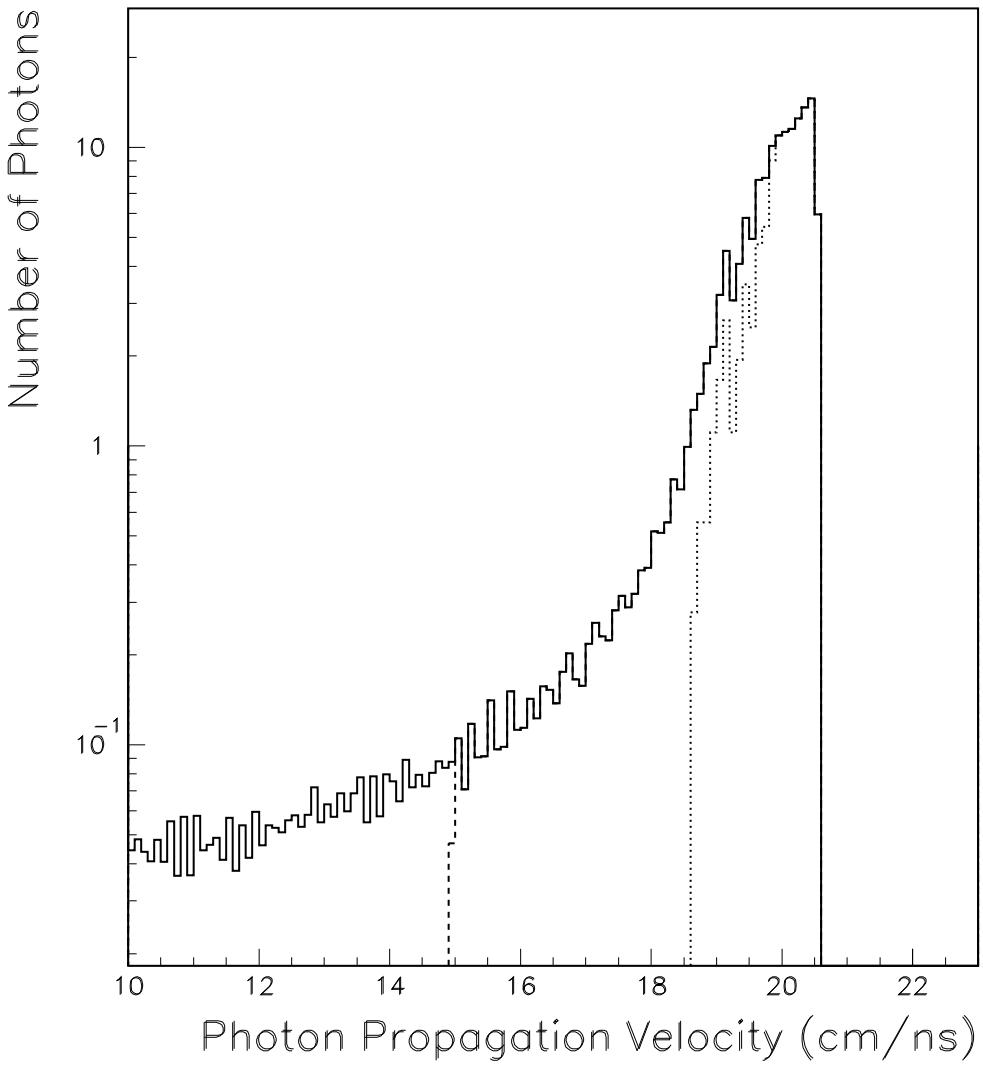
Number of Photons
10
1
10^{-1}
10
12
14
16
18
20
22
Photon Propagation Velocity (cm/ns)

Figure 8

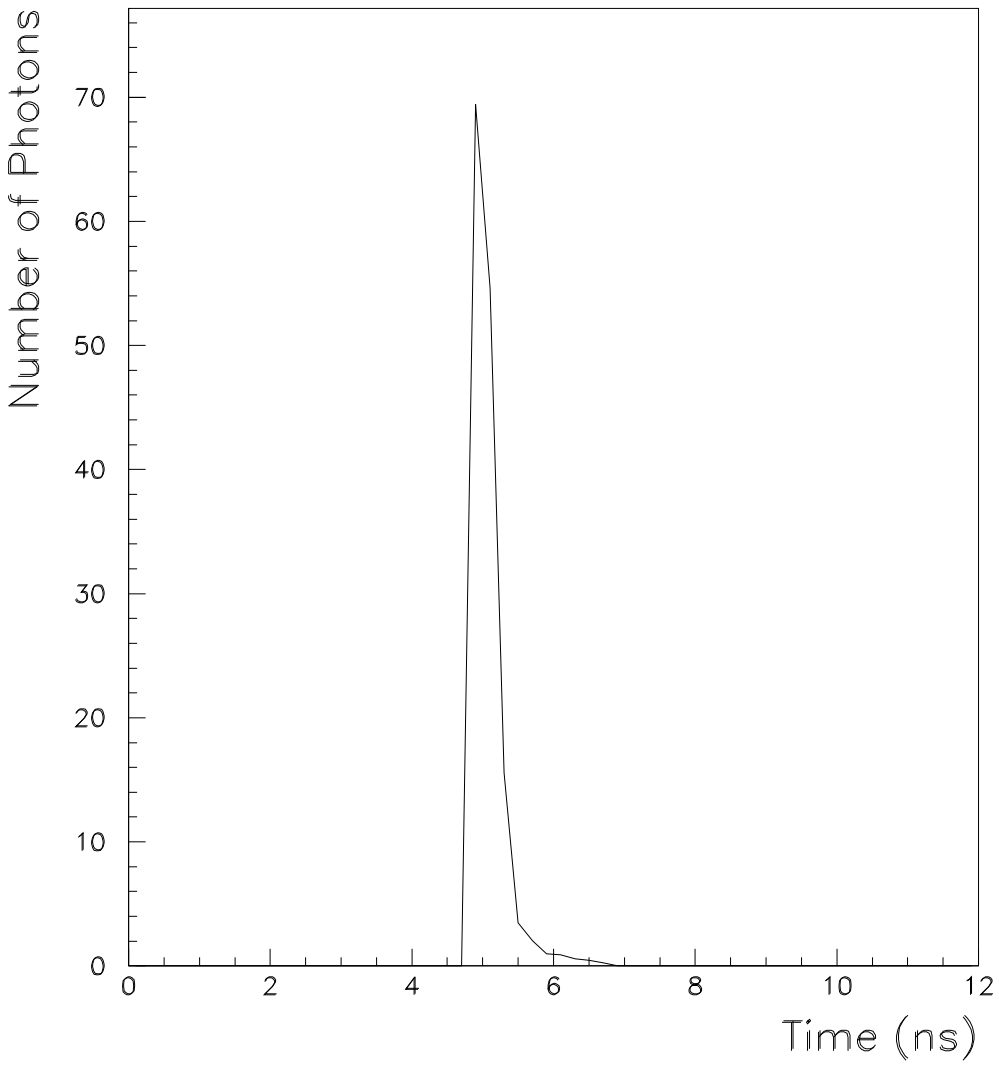

Figure 9

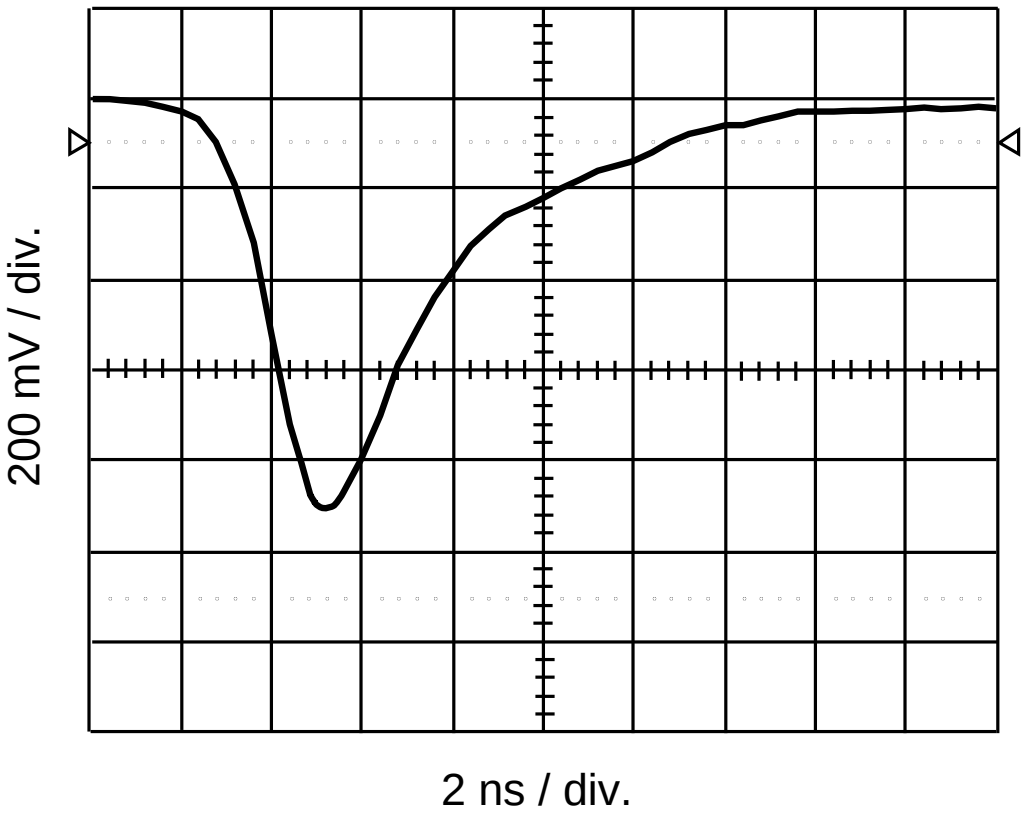

Figure 10

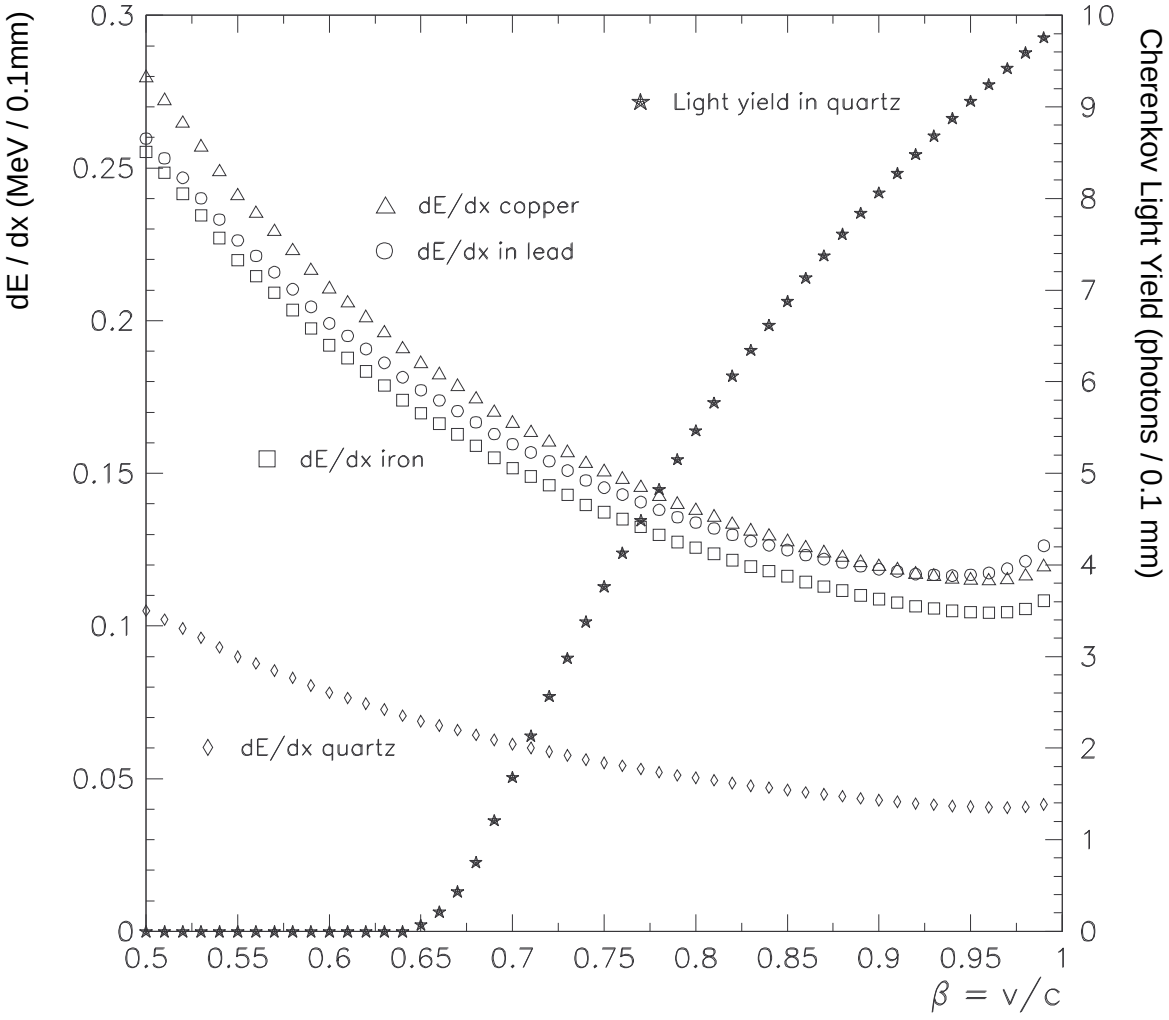
dE / dx (MeV / 0.1mm)
Cherenkov Light Yield (photons / 0.1 mm)
Light yield in quartz
dE/dx copper
dE/dx in lead
dE/dx iron
dE/dx quartz
β = v/c
0.3
0.25
0.2
0.15
0.1
0.05
0
10
9
8
7
6
5
4
3
2
1
0
0.5
0.55
0.6
0.65
0.7
0.75
0.8
0.85
0.9
0.95
1

Figure 11

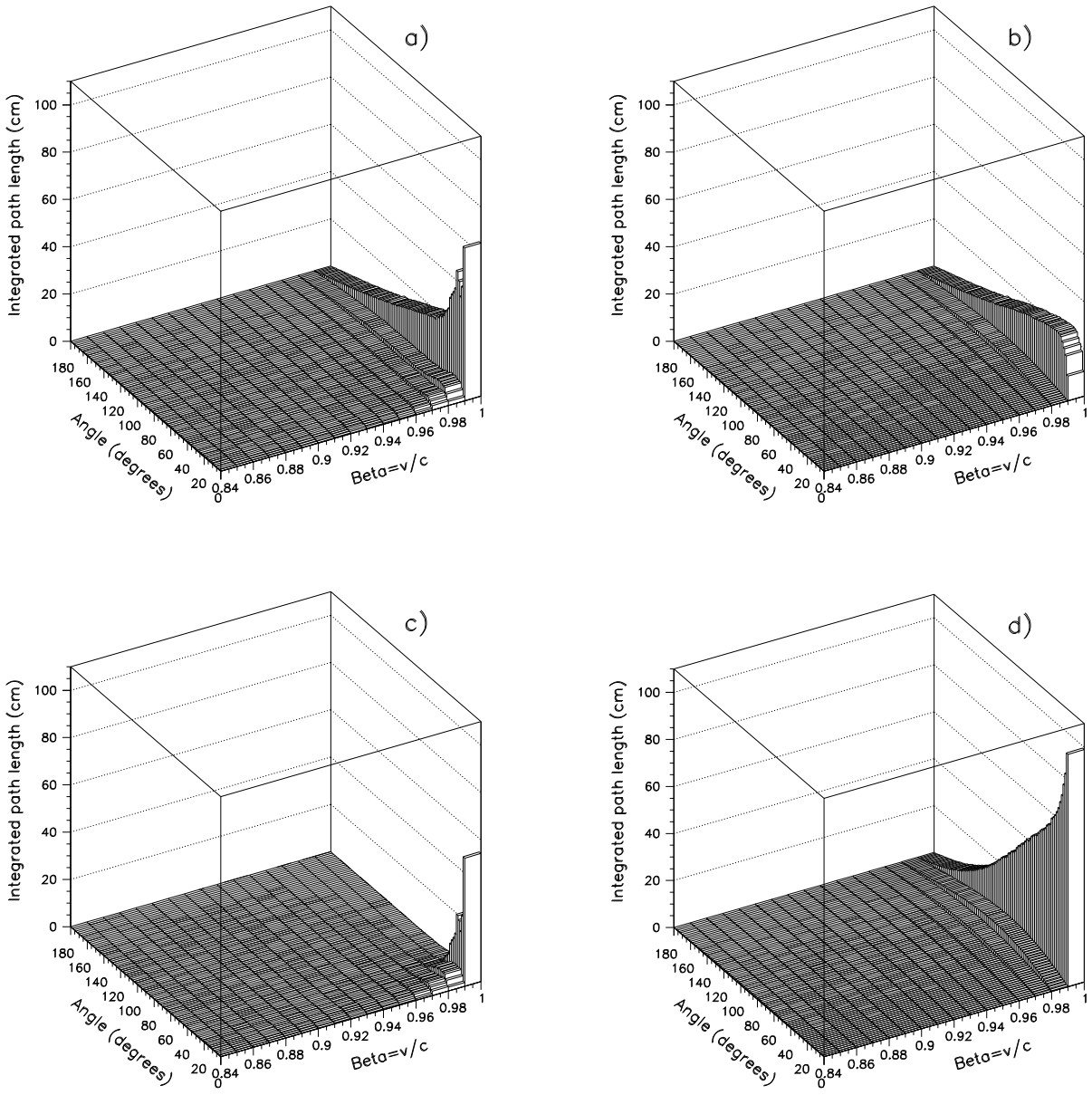

Figure 12

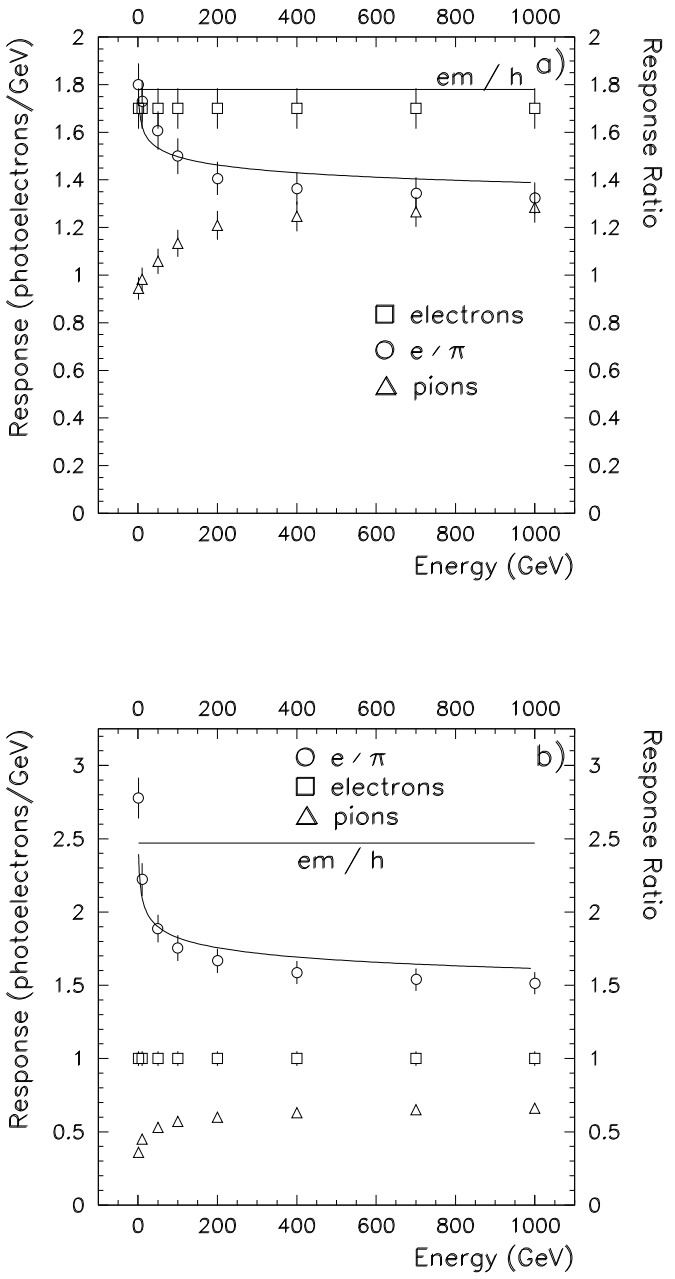
a)
em / h
electrons
e / π
pions
Response (photoelectrons/GeV)
Response Ratio
Energy (GeV)
b)
e / π
electrons
pions
em / h
Response (photoelectrons/GeV)
Response Ratio
Energy (GeV)

Figure 13

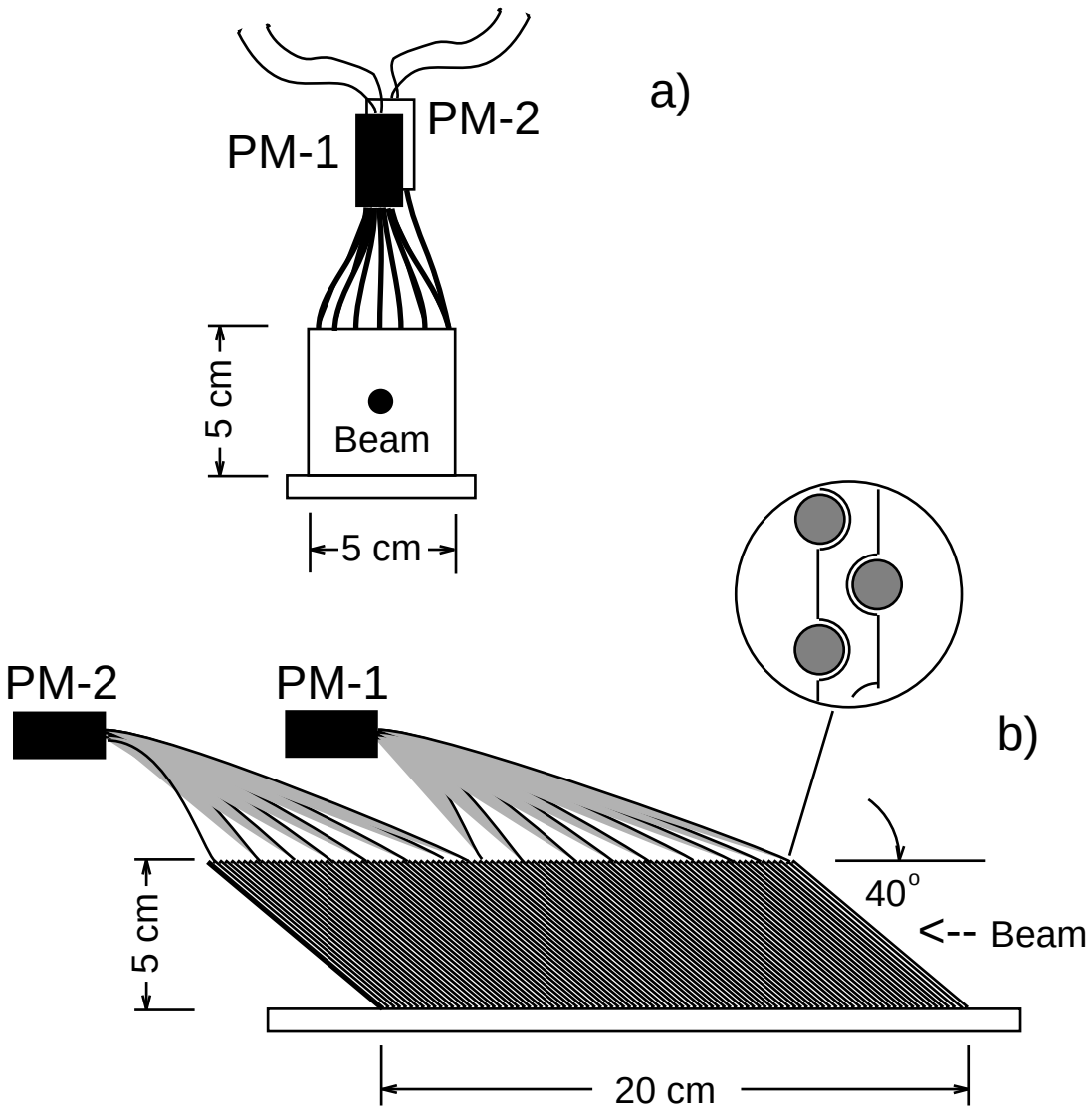

Figure 14

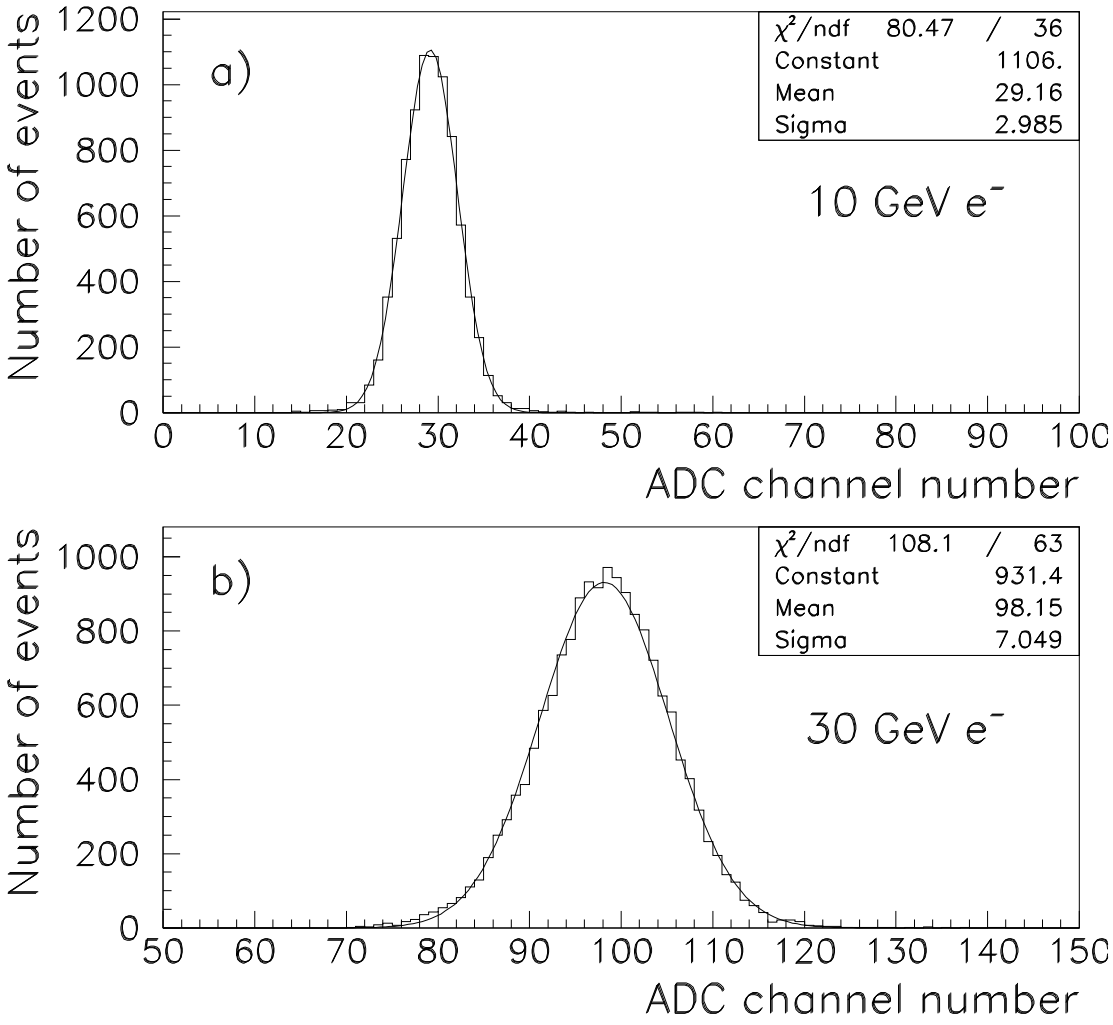
a)
χ^2/ndf 80.47 / 36
Constant 1106.
Mean 29.16
Sigma 2.985
10 GeV e⁻
Number of events
ADC channel number
b)
χ^2/ndf 108.1 / 63
Constant 931.4
Mean 98.15
Sigma 7.049
30 GeV e⁻
Number of events
ADC channel number

Figure 15

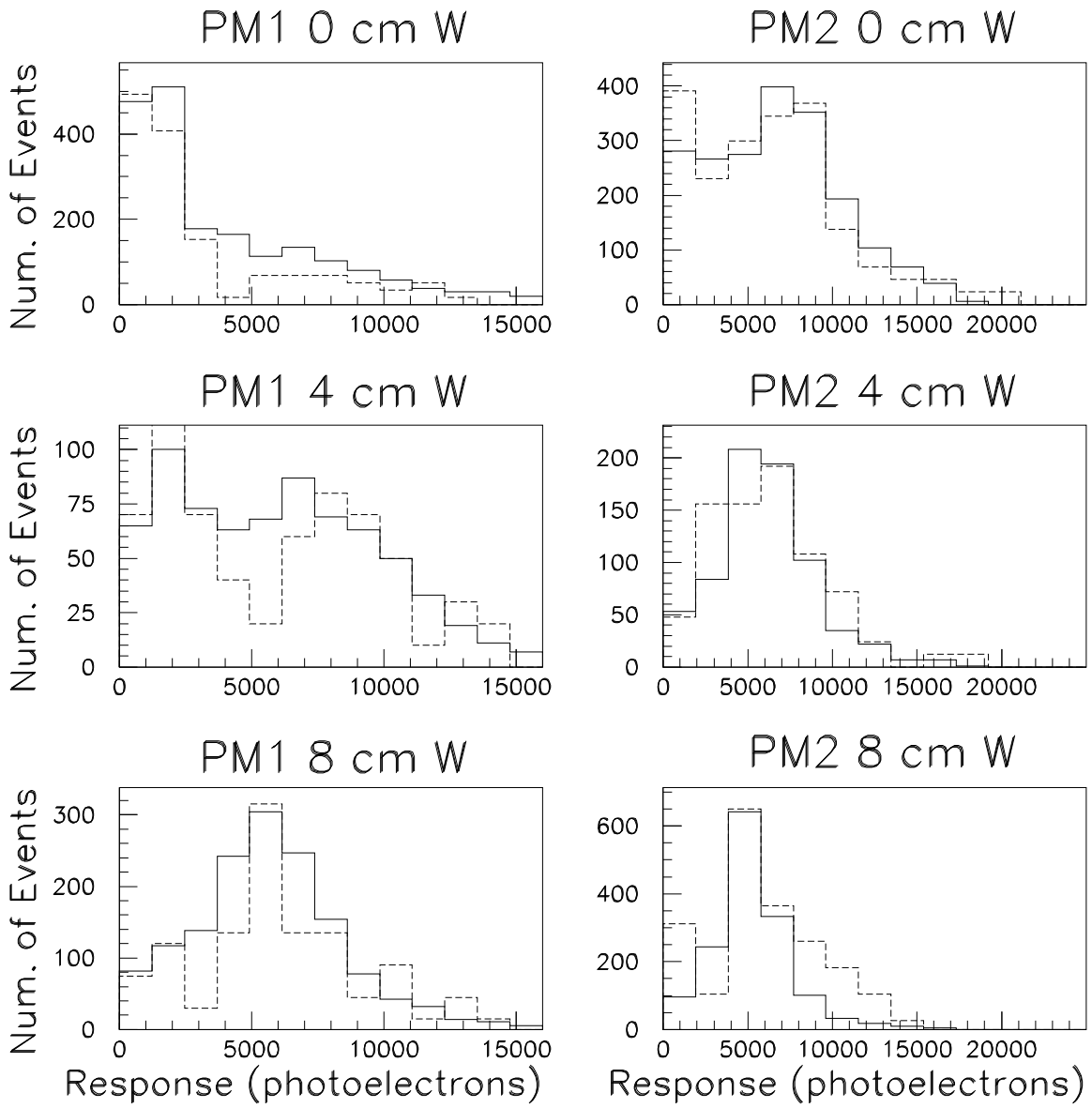
PM1 0 cm W
PM2 0 cm W
PM1 4 cm W
PM2 4 cm W
PM1 8 cm W
PM2 8 cm W
Num. of Events
Response (photoelectrons)
0
5000
10000
15000
20000

Figure 16

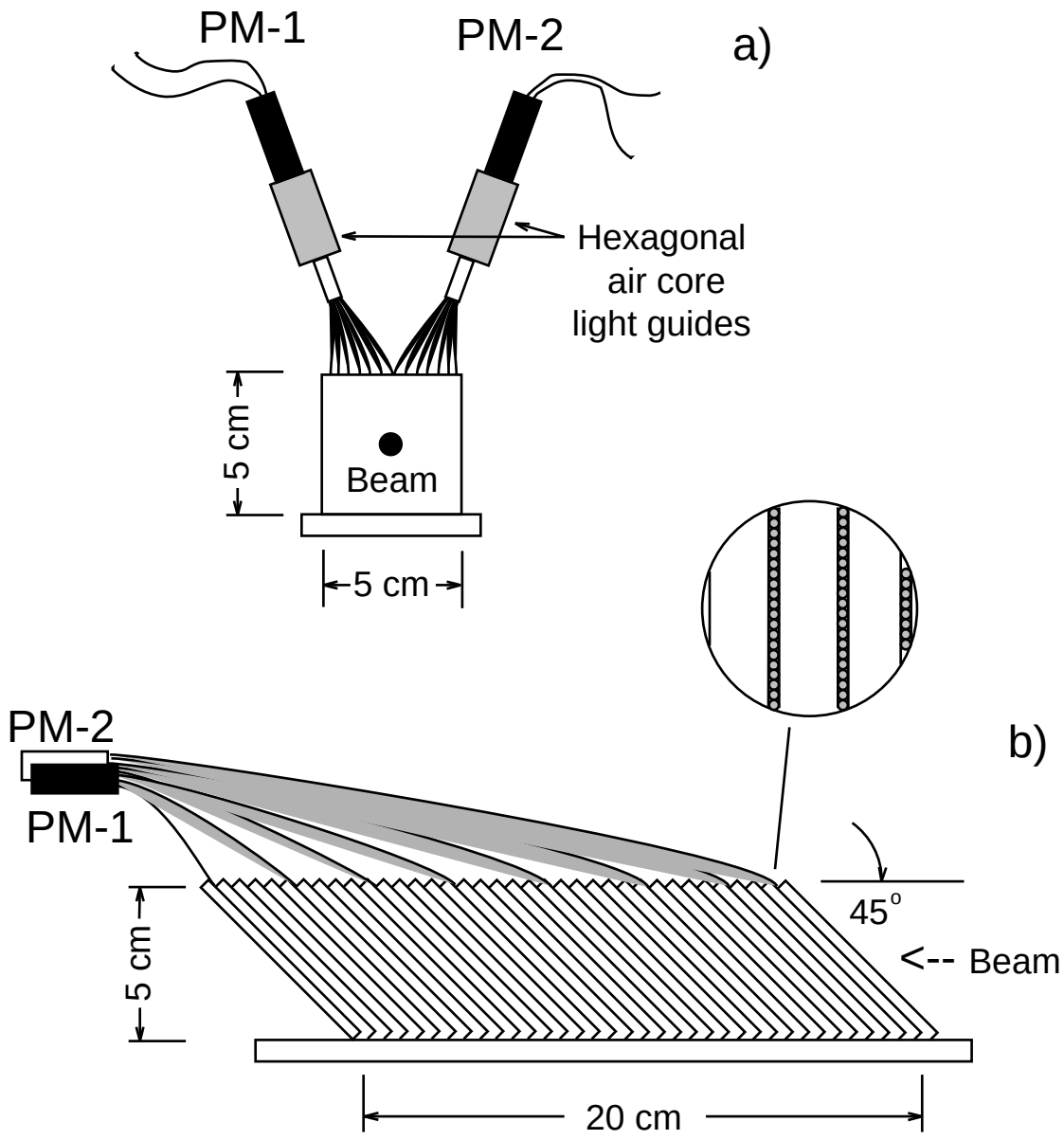
PM-1
PM-2
a)
Hexagonal
air core
light guides
5 cm
Beam
5 cm
PM-2
PM-1
b)
45°
<-- Beam
5 cm
20 cm

Figure 17

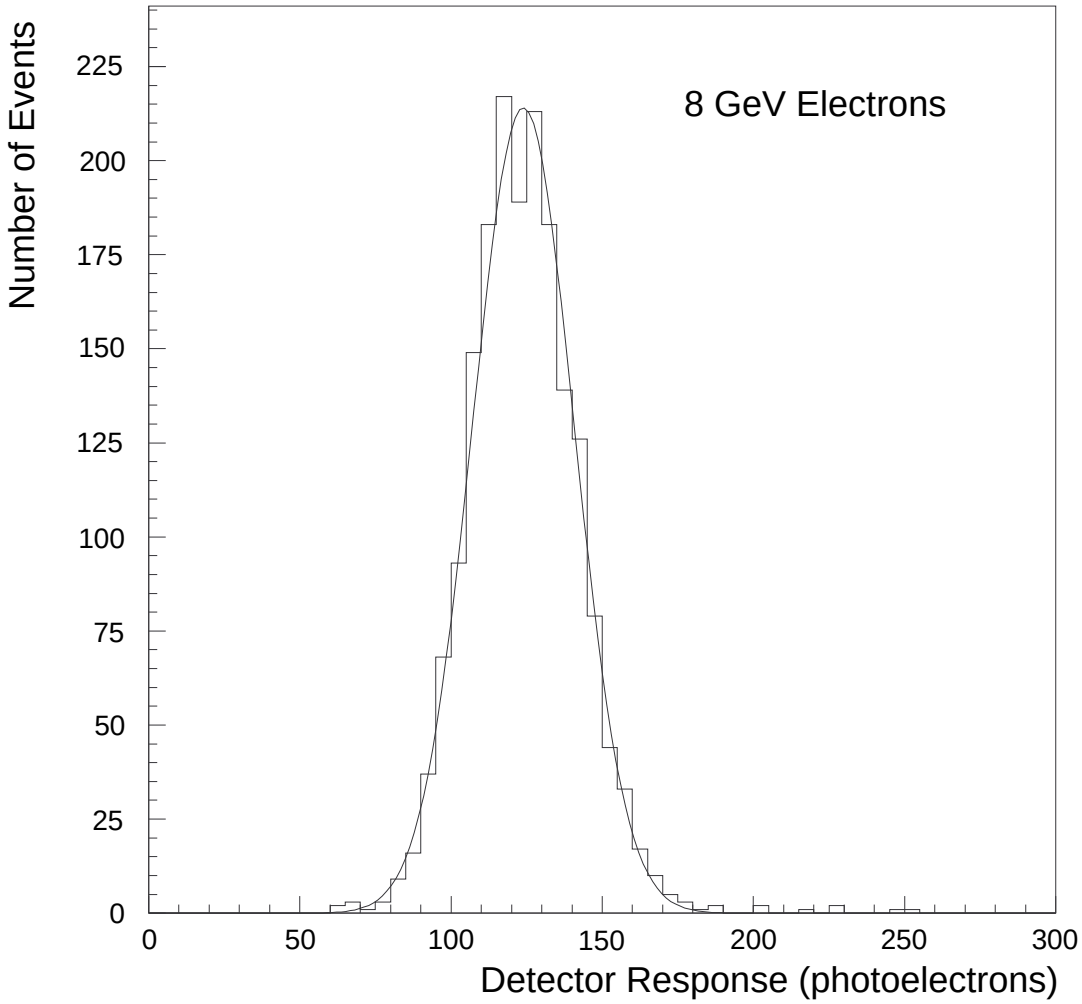
8 GeV Electrons
Number of Events
Detector Response (photoelectrons)
0
25
50
75
100
125
150
175
200
225
0
50
100
150
200
250
300

Figure 18

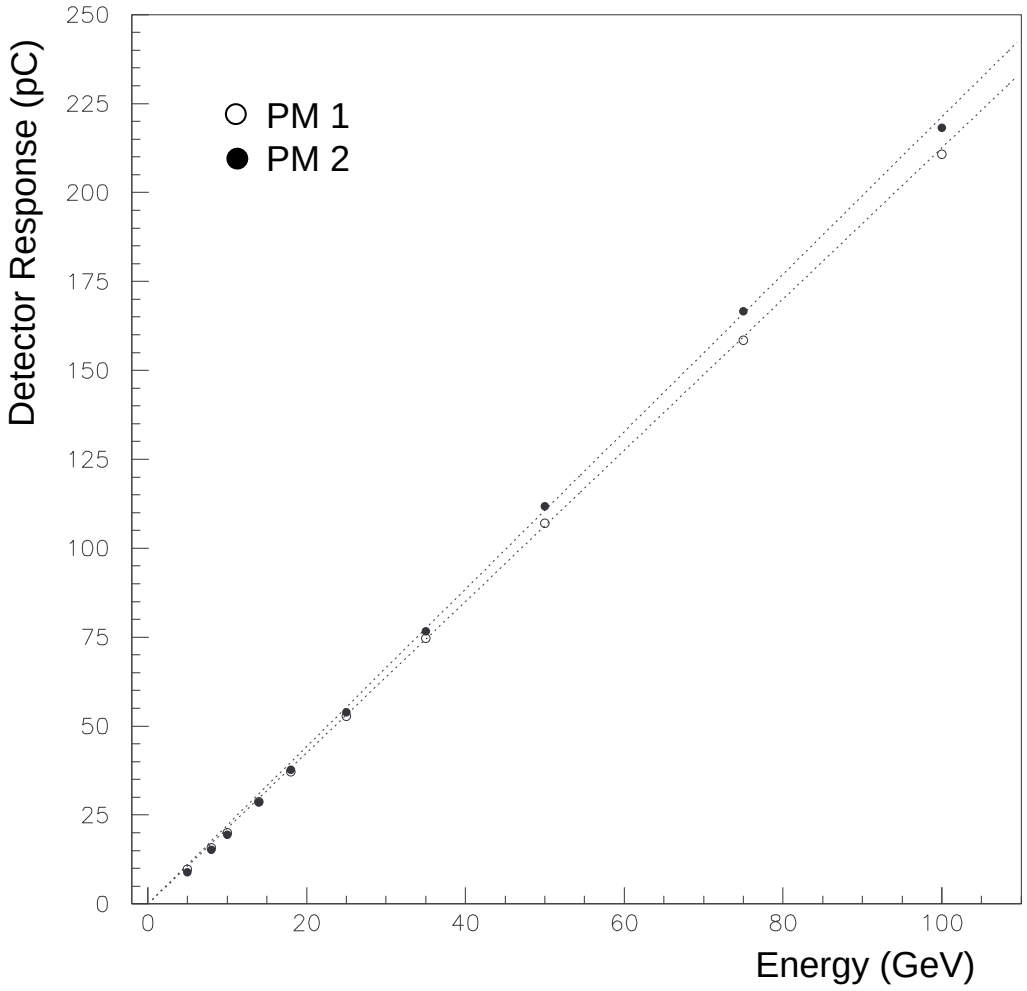
Detector Response (pC)
Energy (GeV)
PM 1
PM 2
0
25
50
75
100
125
150
175
200
225
250
0
20
40
60
80
100

Figure 19

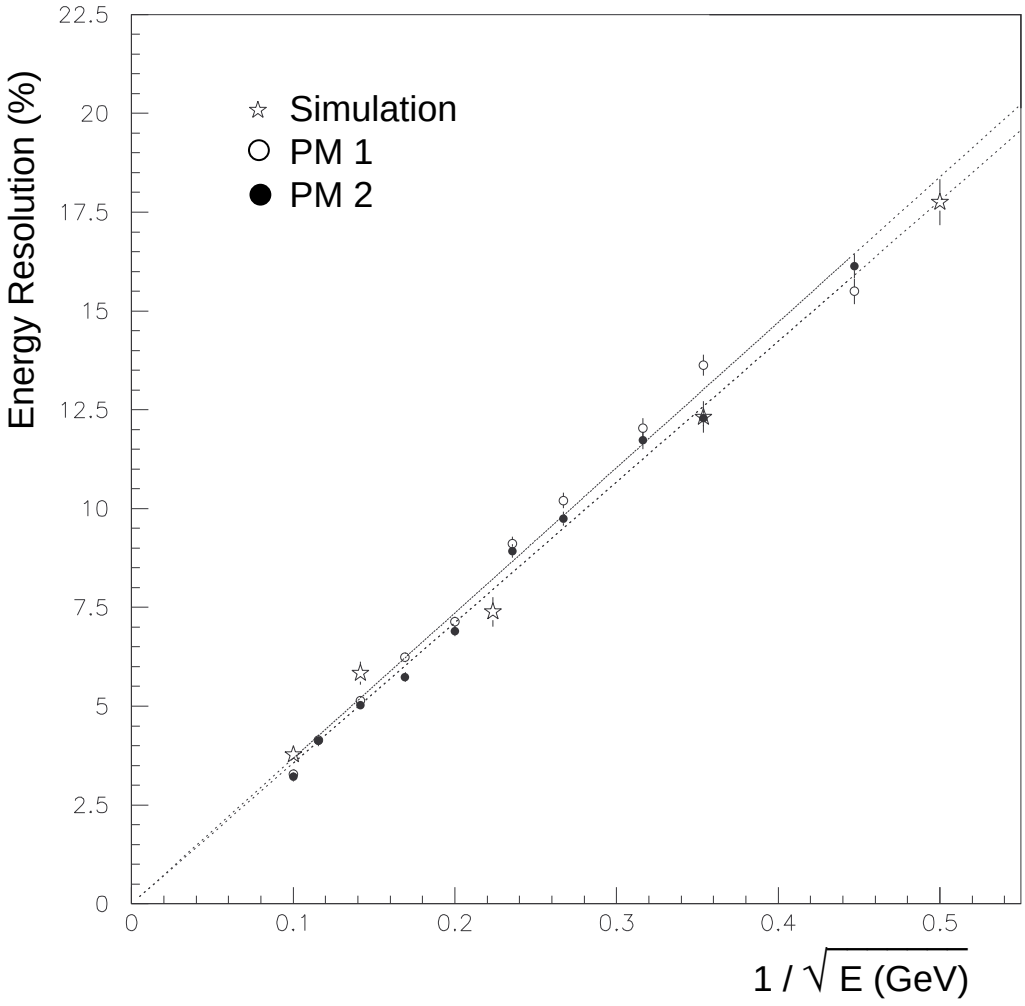
Energy Resolution (%)
22.5
20
17.5
15
12.5
10
7.5
5
2.5
0
Simulation
PM 1
PM 2
0
0.1
0.2
0.3
0.4
0.5
1 / √ E (GeV)

Figure 20

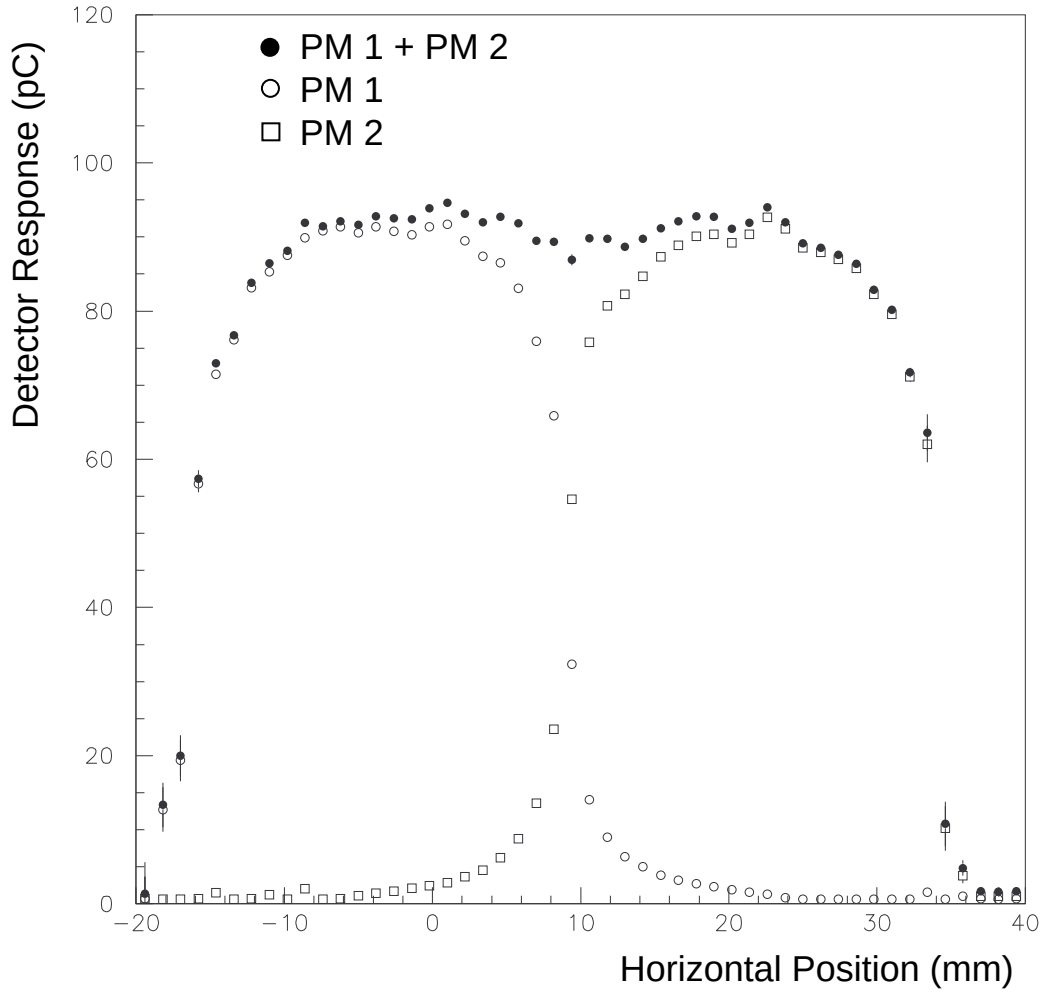
PM 1 + PM 2
PM 1
PM 2
Detector Response (pC)
Horizontal Position (mm)
120
100
80
60
40
20
0
−20
−10
0
10
20
30
40

Figure 21

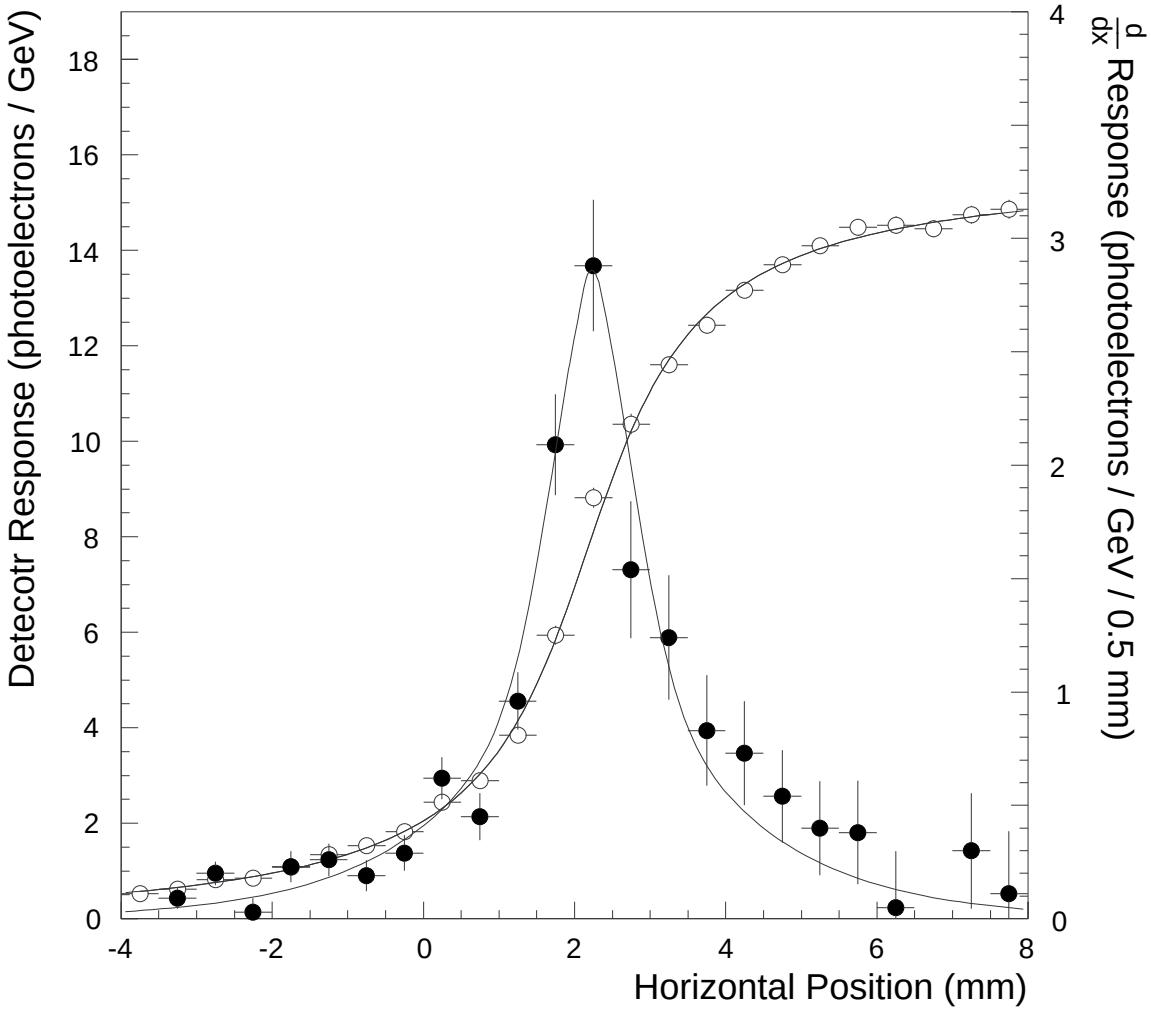
Detecotr Response (photoelectrons / GeV)
$\frac{d}{dx}$ Response (photoelectrons / GeV / 0.5 mm)
Horizontal Position (mm)
0
2
4
6
8
10
12
14
16
18
-4
-2
0
2
4
6
8
1
3

Figure 22

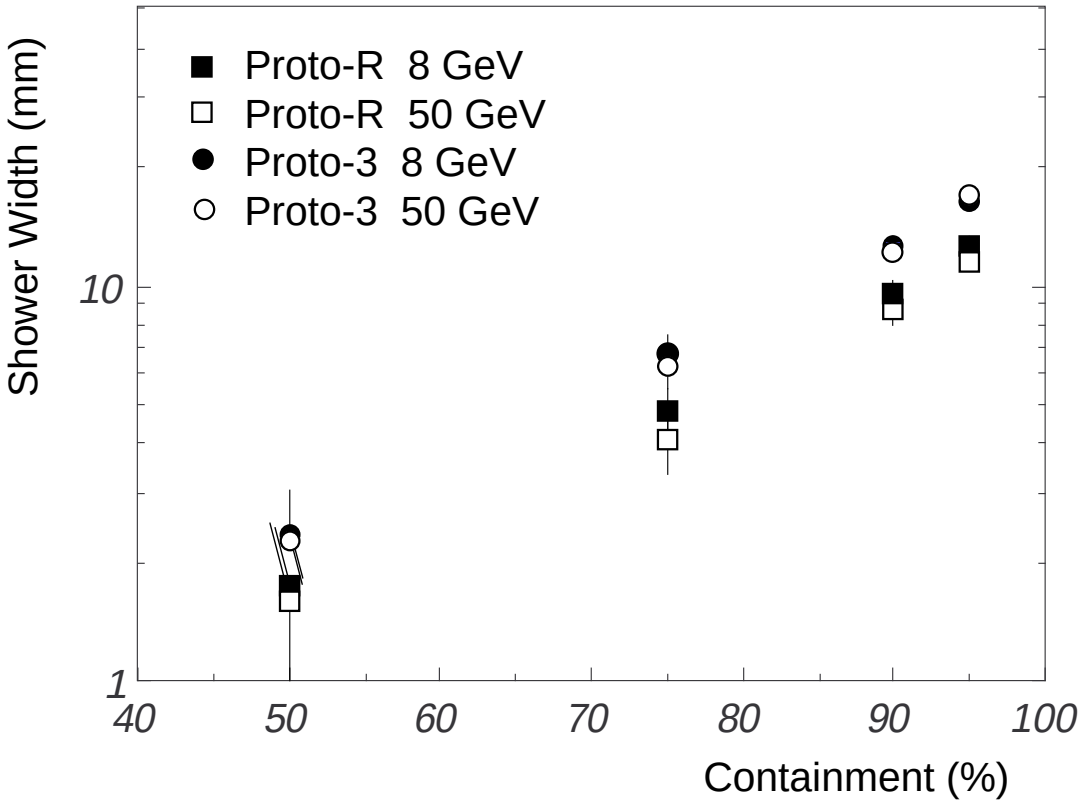
Proto-R 8 GeV
Proto-R 50 GeV
Proto-3 8 GeV
Proto-3 50 GeV
Shower Width (mm)
10
1
40
50
60
70
80
90
100
Containment (%)

Figure 23

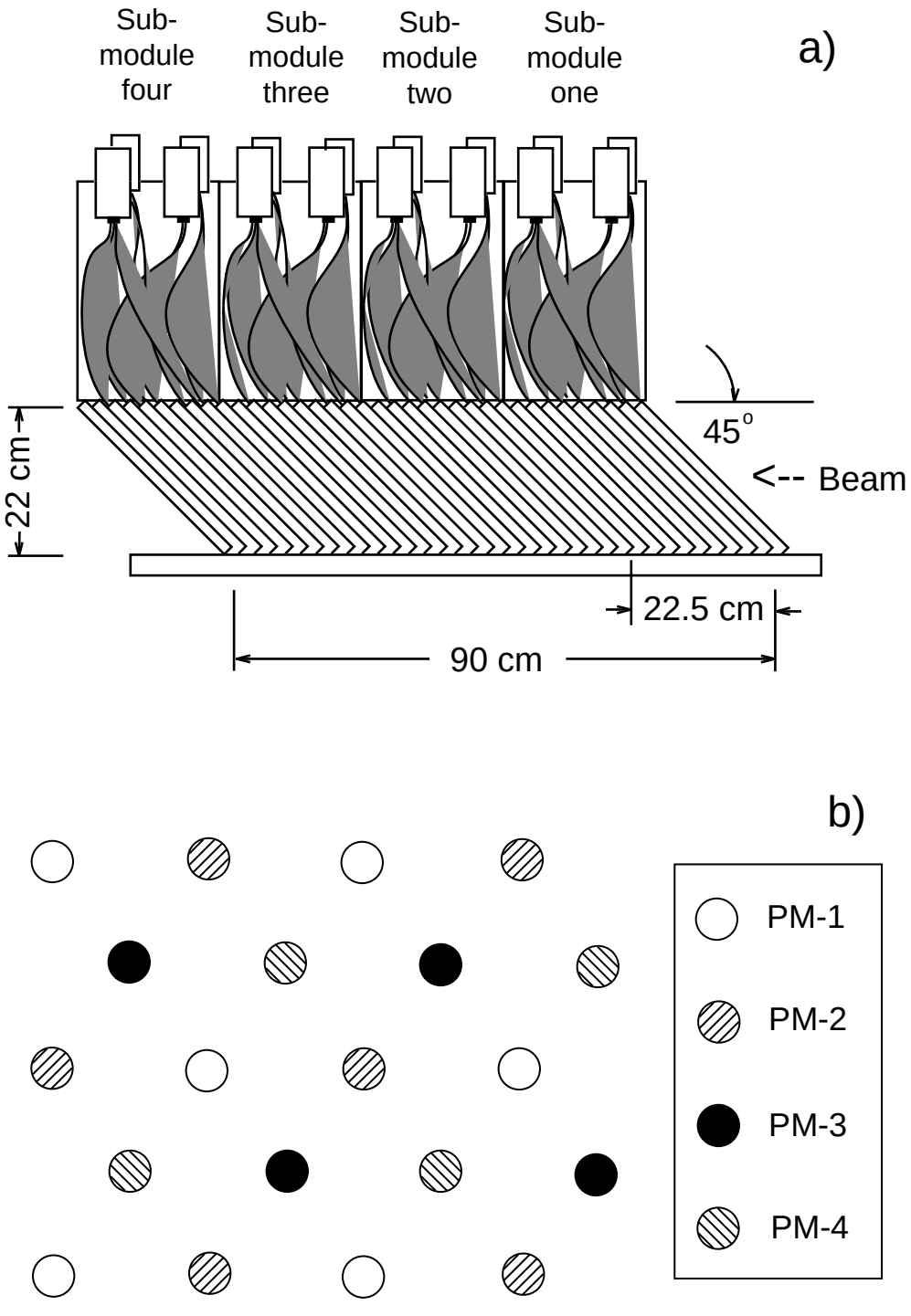
a)
Sub-
module
four
Sub-
module
three
Sub-
module
two
Sub-
module
one
45°
<-- Beam
22 cm
22.5 cm
90 cm
b)
PM-1
PM-2
PM-3
PM-4

Figure 24

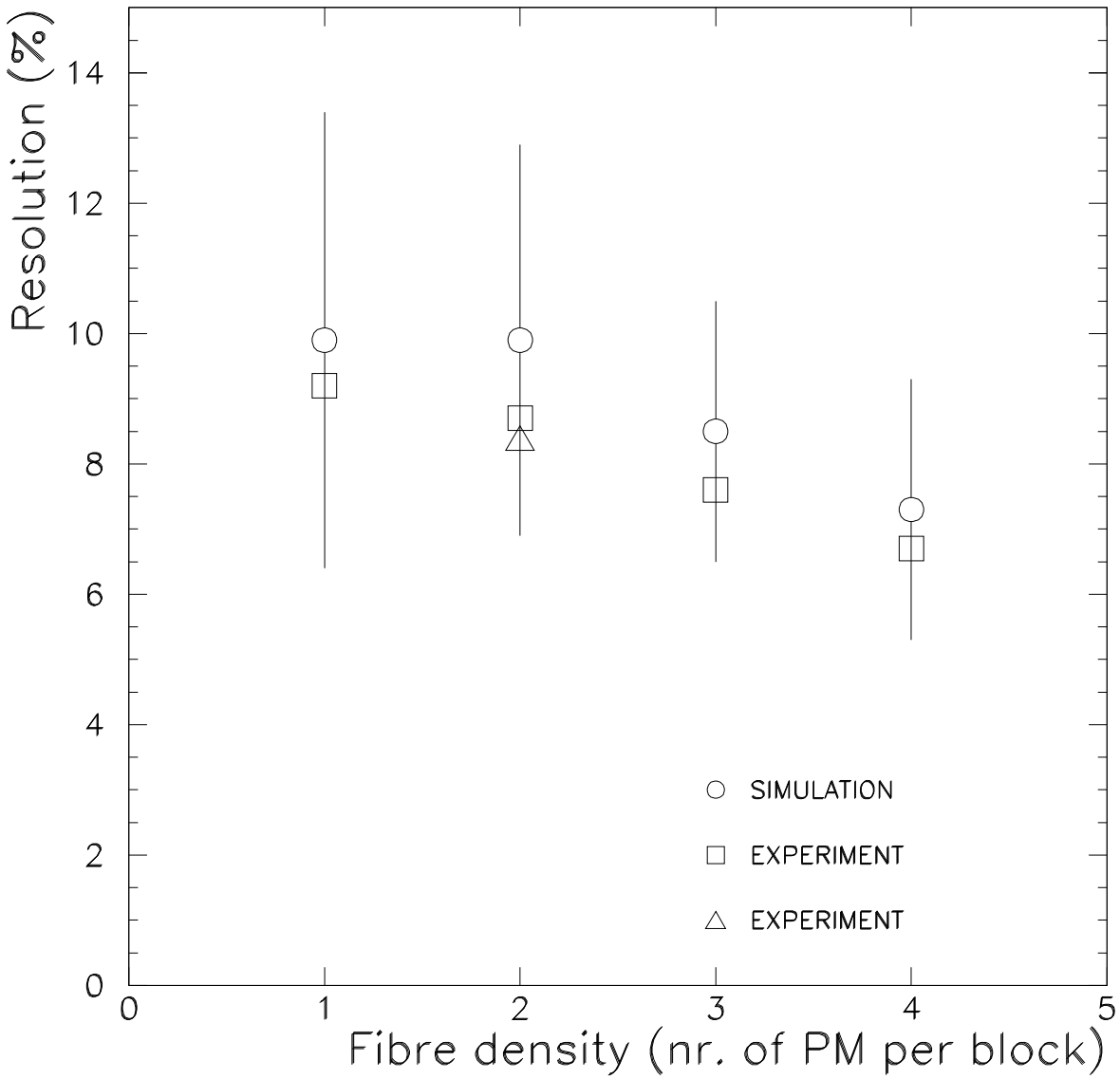
Resolution (%)
0
2
4
6
8
10
12
14
0
1
2
3
4
5
Fibre density (nr. of PM per block)
SIMULATION
EXPERIMENT
EXPERIMENT

Figure 25

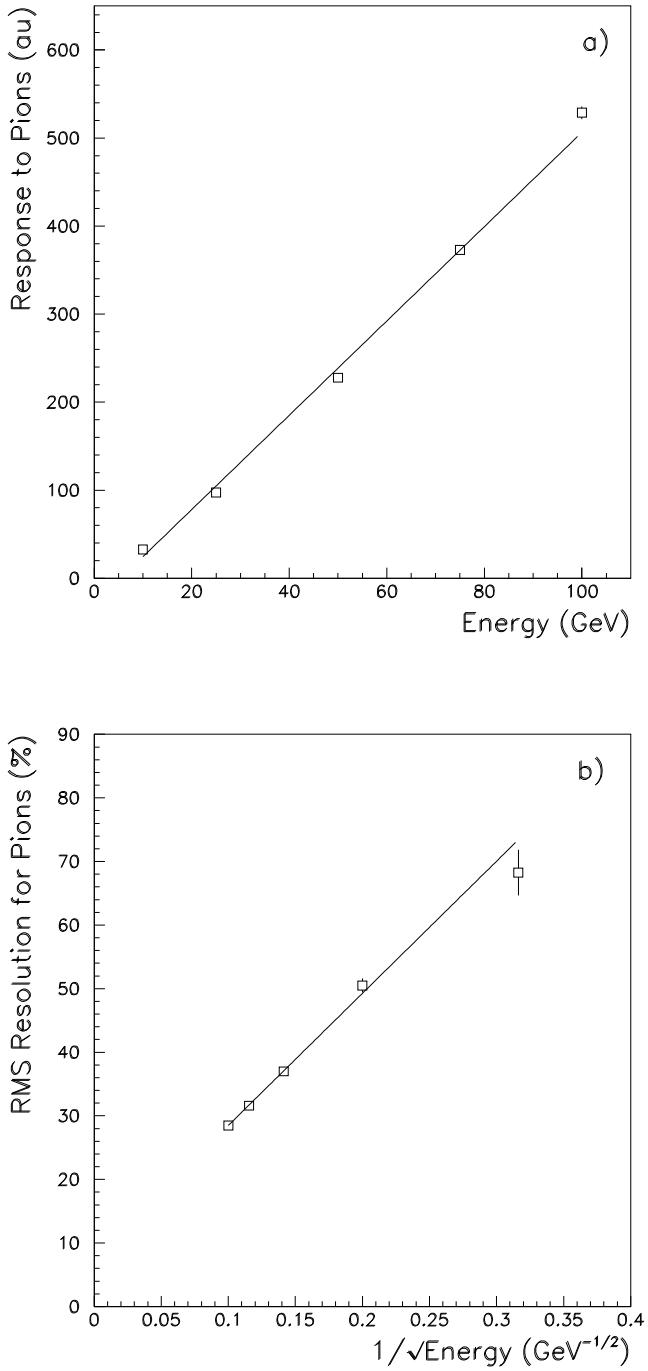
a)
Response to Pions (au)
0
100
200
300
400
500
600
0
20
40
60
80
100
Energy (GeV)
b)
RMS Resolution for Pions (%)
0
10
20
30
40
50
60
70
80
90
0
0.05
0.1
0.15
0.2
0.25
0.3
0.35
0.4
1/√Energy (GeV$^{-1/2}$)

Figure 26

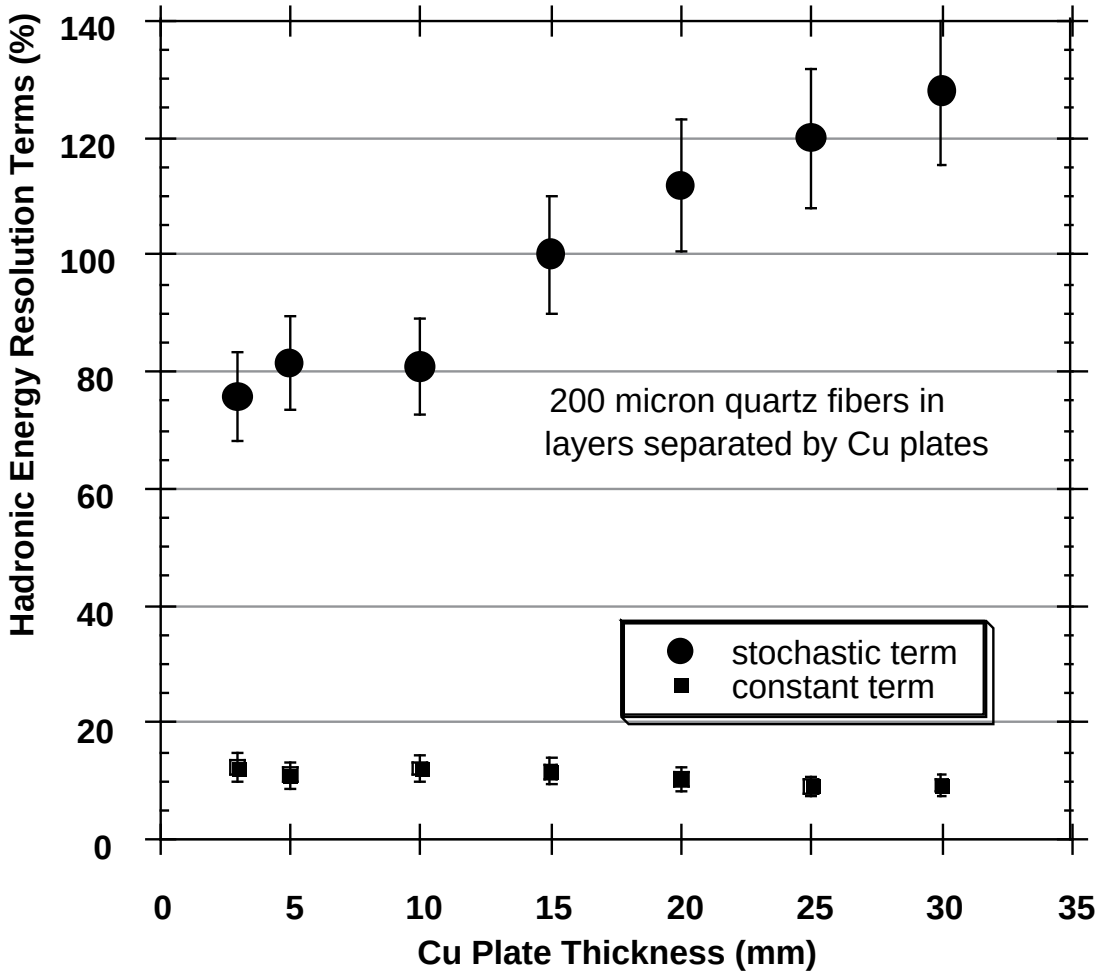
Hadronic Energy Resolution Terms (%)
140
120
100
80
60
40
20
0
0
5
10
15
20
25
30
35
Cu Plate Thickness (mm)
200 micron quartz fibers in
layers separated by Cu plates
stochastic term
constant term

Figure 27

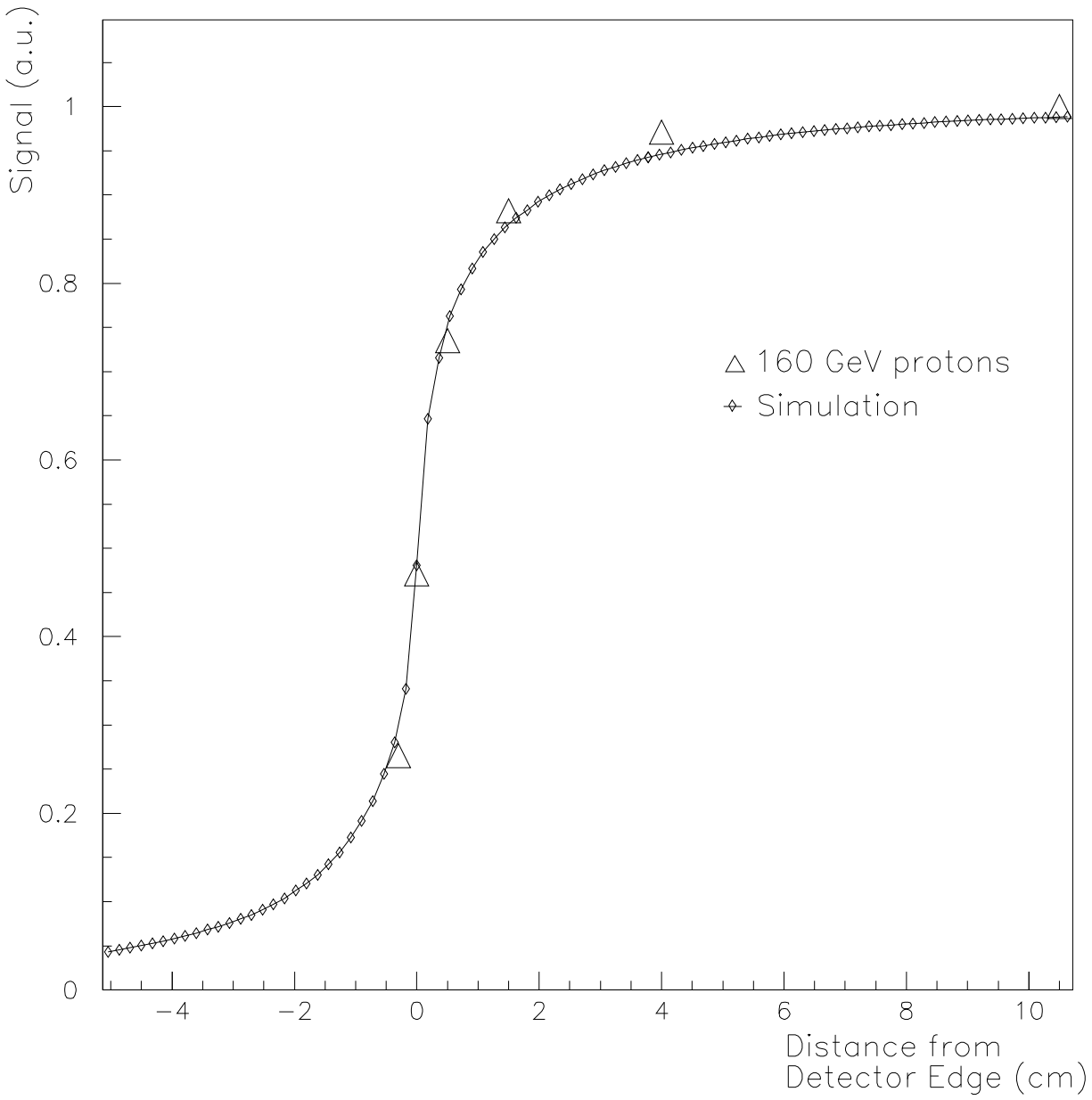
Signal (a.u.)
1
0.8
0.6
0.4
0.2
0
−4
−2
0
2
4
6
8
10
Distance from
Detector Edge (cm)
△ 160 GeV protons
Simulation

Figure 28

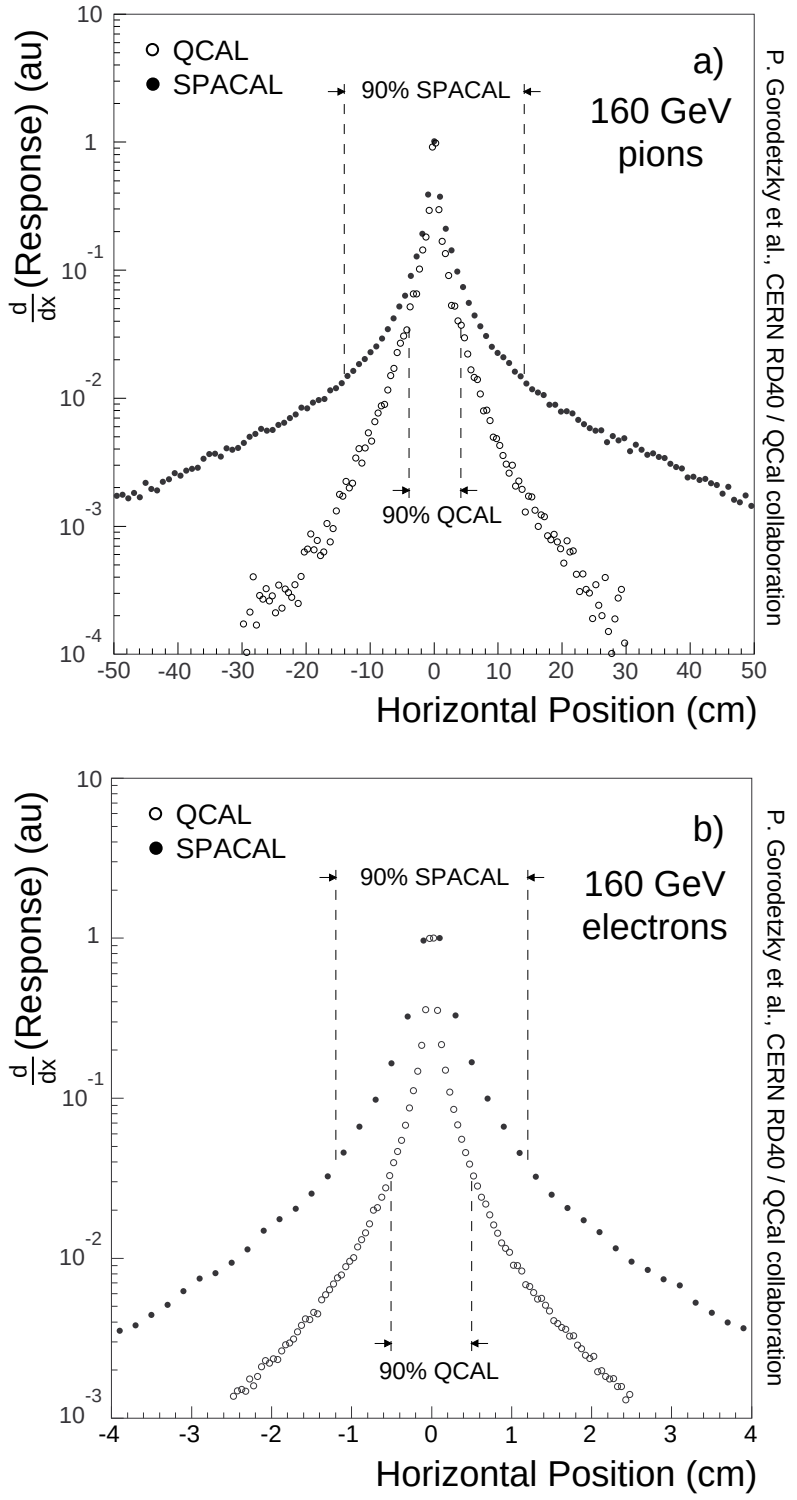
QCAL
SPACAL
90% SPACAL
90% QCAL
a)
160 GeV
pions
d/dx (Response) (au)
Horizontal Position (cm)
P. Gorodetzky et al., CERN RD40 / QCal collaboration
b)
160 GeV
electrons

Figure 29